Diffusion Tensor Magnetic Resonance Imaging : Brain Connectivity Mapping

Christophe Lenglet, Rachid Deriche, Olivier Faugeras

INSTITUT NATIONAL DE RECHERCHE EN INFORMATIQUE ET EN AUTOMATIQUE

Diffusion Tensor Magnetic Resonance Imaging: Brain Connectivity Mapping

Christophe LENGLET — Rachid DERICHE — Olivier FAUGERAS

N° 4983

October 31, 2003

THÈME 3

ISSN 0249-6399 ISRN INRIA/RR--4983--FR+ENG

INRIA
SOPHIA ANTIPOLIS

Diffusion Tensor Magnetic Resonance Imaging: Brain Connectivity Mapping

Christophe LENGLET* , Rachid DERICHE† , Olivier FAUGERAS‡

Thème 3 — Interaction homme-machine,
images, données, connaissances
Projet Odyssée

Rapport de recherche n° 4983 — October 31, 2003 — 40 pages

Abstract: Diffusion tensor MRI probes and quantifies the anisotropic diffusion of water molecules in biological tissues, making it possible to non-invasively infer the architecture of the underlying structures. We introduce a novel approach to the cerebral white matter connectivity mapping from diffusion tensor MRI. We address the problem of consistent neural fibers reconstruction in areas of complex diffusion profiles with potentially multiple fibers orientations. Our method relies on a global modelization of the acquired MRI volume as a Riemannian manifold M and proceeds in 4 majors steps:
1. We establish the link between Brownian motion and diffusion MRI by using the Laplace-Beltrami operator on M.
2. We then expose how the sole knowledge of the diffusion properties of water molecules on M is sufficient to infer its geometry. There exists a direct mapping between the diffusion tensor and the metric of M.
3. Having access to that metric, we propose a novel level set formulation to approximate the distance function related to a radial Brownian motion on M.
4. On that basis, a rigorous numerical scheme using the exponential map is derived to estimate the geodesics of M, seen as the diffusion paths of water molecules.
Numerical experimentations conducted on synthetic and real diffusion MRI datasets illustrate the potentialities of this global approach.

Key-words: diffusion tensor MRI, brain connectivity mapping, tractography, Brownian motion, diffusion process, Laplace-Beltrami operator, differential geometry, intrinsic distance function, geodesics, anisotropic eikonal equation, level sets

* Christophe.Lenglet@sophia.inria.fr
† Rachid.Deriche@sophia.inria.fr
‡ Olivier.Faugeras@sophia.inria.fr

Unité de recherche INRIA Sophia Antipolis
2004, route des Lucioles, BP 93, 06902 Sophia Antipolis Cedex (France)
Téléphone : +33 4 92 38 77 77 —Télécopie : +33 4 92 38 77 65

Imagerie par Résonance Magnétique du Tenseur de Diffusion: Cartographie de la Connectivité Cérébrale

Résumé : L'IRM du tenseur de diffusion quantifie l'anisotropie de la diffusion des molécules d'eau dans les tissus biologiques, rendant possible l'inférence non-invasive de l'architecture des structures sous-jascentes. Nous introduisons une nouvelle approche pour la cartographie de la connectivité anatomique dans la matière blanche basée sur le tenseur de diffusion. Nous adressons le problème de la reconstruction cohérente des fibres neuronales dans les régions dont le profile de diffusion s'avère complexe et peut traduire l'existence de plusieurs orientations. Notre méthode s'appuie sur une modélisation globale du volume IRM par une variété Riemannienne M et procède en 4 étapes:
1. Nous établissons le lien entre mouvement Brownien et IRM de diffusion via l'opérateur de Laplace-Beltrami sur M.
2. Nous exposons ensuite comment la seule connaissance des propriétés de diffusion des molécules d'eau sur M suffit à en déduire sa géométrie. Il existe une correspondance directe entre le tenseur de diffusion et la métrique de M.
3. Ayant accès à cette métrique, nous proposons une formulation utilisant le cadre théorique des ensembles de niveau pour approximer la fonction distance associée à un mouvement Brownien radial sur M.
4. Enfin, un schéma numérique rigoureux utilisant les cartes exponentielles est dérivé pour calculer les géodésiques de M, considérées comme les chemins de diffusion des molécules d'eau.
Les expérimentations numériques conduites sur des données synthétiques et réelles illustrent les capacités de cette approche globale.

Mots-clés : IRM du tenseur de diffusion, cartographie de la connectivité cérébrale, mouvement Brownien, processus de diffusion, operateur de Laplace-Beltrami, géométrie différentielle, fonction distance intrinsèque, géodésiques, équation eikonale anisotrope, ensembles de niveau

Contents

1 Introduction

Diffusion imaging is a magnetic resonance imaging technique introduced in the mid 1980s [40], [50] which provides a very sensitive probe of biological tissues architecture. Although this method suffered, in its very first years, from severe technical constraints such as acquisition time or motion sensitivity, it is now taking an increasingly important place with new acquisition modalities such as ultrafast echo-planar methods.

Regular MRI techniques enable us to easily and automatically distinguish and classify gray matter, white matter and cephalo-spinal fluid. However, white matter does retain an homogeneous aspect, preventing any observation of neural fibers and thus of neuronal connectivity. In order to understand the neural fibers bundle architecture, anatomists used to perform cerebral dissection [23], strychnine or chemical markers neuronography [66], [70]. More recently neural pathways tracking based on local injection of chemical markers, and *a posteriori* observation of the induced propagation yielded high-quality connectivity mapping in the cat and monkey cerebral cortex [90], [70]. As of today, diffusion MRI is the unique non-invasive technique capable of probing and quantifying the anisotropic diffusion of water molecules in tissues like brain or muscles. As we will see in the following, the diffusion phenomenon is a macroscopic physical process resulting from the random walk of these molecules. All microscopic particles permanently undergo a translation and rotation motion due to their thermal energy and also known as Brownian motion. This microscopic phenomenon, related to the bombardment by molecules obeying a Maxwellian velocity distribution, was better understood by A. Einstein in 1905 and identified as depending on temperature and viscosity of the domain as well as particles size. Diffusion shows, at a broader scale, how molecules tend to move from low concentration areas to high concentration areas over distances of about 10 to 15 μm during typical times of 50 to 100 ms. The key concept that is of primary importance for diffusion imaging is that diffusion in biological tissues reflects their structure and their architecture at a microscopic scale. For instance, Brownian motion is highly influenced in tissues such as cerebral white matter or the *annulus fibrosus* of inter-vertebral discs. Measuring, at each voxel, that very same motion along a number of sampling directions (at least 6, up to several hundreds) provides an exquisite insight into the local orientation of fibers and is known as diffusion-weighted imaging. Shortly after the first acquisitions of images characterizing the anisotropic diffusion of water molecules *in vivo* [54], [59] Basser et al. [6], [7] proposed in 1994 the model, now widely used, of the diffusion tensor featuring an analytic means to precisely describe the three-dimensional nature of anisotropy in tissues.

Numerous works have already addressed the problem of the estimation and regularization of the diffusion tensor fields. References can be found in [81], [21], [89], [86]. Motivated by the potentially dramatic improvements that knowledge of anatomical connectivity would bring into the understanding of functional coupling between cortical regions [28], the study of neurodegenerative diseases, acute brain ischemia detection [1], [87], [73], neurosurgery planning or tumor growth quantification, various methods have been proposed

to tackle the issue of cerebral connectivity mapping.
Local approaches based on line propagation techniques [52], [91] provide fast algorithms and have been augmented to incorporate some natural constraints such as regularity, stochastic behavior and even local non-Gaussianity ([39], [8], [48], [14], [82], [29], [11], [60]). All these efforts aim to overcome the intrinsic ambiguity of the diffusion tensor related to white matter partial volume effects. Bearing in mind this limitation, they enable us to generate relatively accurate models of the human brain macroscopic three-dimensional architectures. The tensor indeed encapsulates the averaged diffusion properties of water molecules inside a voxel whose typical extents vary from 1 to 3 mm. At this resolution, the contribution to the measured anisotropy of a voxel is very likely to come from different fibers bundles presenting different orientations. This voxel-wise homogeneous Gaussian model thus limits our capacity to resolve multiple fibers orientations since local tractography becomes unstable when crossing artificially isotropic regions characterized by a planar or spherical diffusion profile [89].
On the other side, *hardware* solutions have been recently introduced in an attempt to better describe the complexity of water motion but at the cost of increased acquisition times. This is the case of high angular diffusion weighted imaging [83], [26] where the variance of the signal could give important information on the multimodal aspect of diffusion. Diffusion Spectrum Imaging [84], [43] provides, at each voxel, an estimation of the probability density function of water molecules and has been shown to be a particularly accurate means to access the whole complexity of the diffusion process in biological tissues. In favor of these promising modalities, parallel MRI [3] will reduce the acquisition time in a near future and thus permit high resolution imaging.

More global algorithms have been proposed to better handle the situations of false planar or spherical tensors (with underlying fibers crossings) and to propose some sort of likelihood of connection. However, they either make use of the major eigenvector field [61], [17] or consider the evolution of a front in Euclidean space while adapting its speed through the use of the complete diffusion tensor [56]. In this last attempt, the diffusion tensor is used to compute the metric of a Riemannian manifold but the geometry of that manifold was not exploited.

We derive a novel approach to white matter analysis, through the use of stochastic processes and differential geometry which yield physically motivated distance maps in the brain, seen as a 3-manifold and thus the ability to compute intrinsic geodesics in the white matter. Our goal is to recast the challenging task of connectivity mapping into the natural framework of Riemannian differential geometry. Chapter 2 recalls important facts on Magnetic Resonance Imaging and molecular diffusion in the context of white matter anatomy. It shows the links of Brownian motion with the diffusion MRI signal for linear spaces in terms of its probability density function. Generalization to manifolds will involve the introduction of the infinitesimal generator of the Brownian motion. Chapter 3 describes and analyses classical algorithms for neural pathways computation. It then solves the

problem of computing the intrinsic distance function from a starting point x_0 in the white matter understood as a manifold. The key idea is that the geometry of the manifold M has a deep impact on the behavior of Brownian motion. We claim that the diffusion tensor can be used to infer geodesic paths on M that coincide with neural tracts since its inverse defines the metric of M. Practically, this means that, being given any subset of voxels in the white matter, we will be able to compute paths most likely followed by water molecules to reach x_0. As opposed to many methods developed to perform tractography, we can now exhibit a bunch of fibers starting from a single point x_0 and reaching potentially large areas of the brain. Efficient numerical implementation is non-trivial and described at the end of Chapter 3. Results, advantages and drawbacks of the method are presented and discussed. We finally conclude and present potential extensions of the method.

2 From Molecular Diffusion to Anatomical Connectivity

The human brain, according to the connectionist point of view, is organized into distinct processing regions interconnected by a network of anatomical relays. The processing units handle the execution of primary cognitive functions and higher cognitive tasks arise from a global coordination between those processing units. Neural signal is processed in the cerebral cortex and transmitted to various regions of the brain through the white matter, so called because of the white appearance of the myelinated axons. The white matter pathways are generally categorized into commissural, association and projection fibers, depending on the areas they connect. Compared to our understanding of neural circuitry in animals such as cat or mouse where the use of invasive tracers is possible [51], our knowledge of the human brain connectivity is relatively poor. Diffusion MRI shall allow us to access this critical information.

2.1 A Quick Tour in Neuroanatomy

The largest part of the human brain, the forebrain, is composed by the cerebrum, the thalamus, the hypothalamus and the limbic system. Moreover, the cerebrum is, in turn, divided into two hemisphere connected by the *corpus callosum*. Roughly speaking, each hemisphere is also divided into four lobes: frontal, parietal, occipital and temporal. The frontal lobe is located in front of the central sulcus and generally associated with reasoning, planning and, partially with speech and movement. The parietal lobe, behind the central sulcus, is concerned with the perception of stimuli like pressure or temperature. The temporal lobe, located below the lateral fissure, plays an important role in perception and recognition of sounds and memory. Finally the occipital lobe, behind the parietal and temporal lobes, is of great importance for vision tasks. White matter, on which we will focus, is mainly located between the cerebral cortex (ie. the surface of each hemisphere) and the basal nuclei, transmitting information between those two structures to perform high-order cognitive tasks. Let us now give a short overview of the three main types of neural tracts in the white matter:

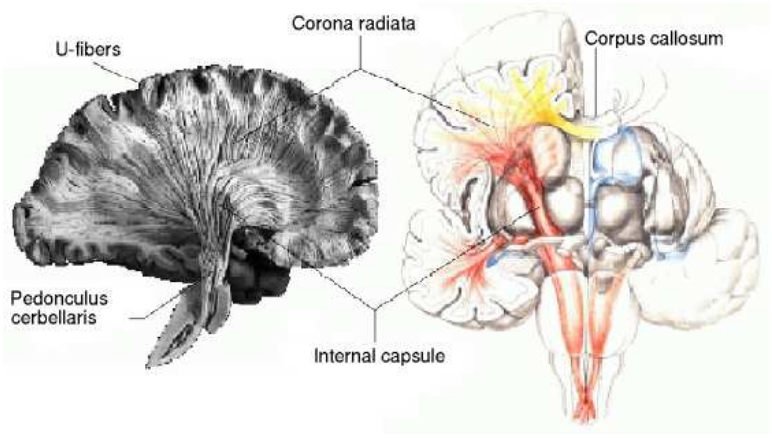

Figure 1: The three different types of axonal tracts (from [64])

Commissural tracts are bundles of axons connecting a region in one hemisphere to another region of the opposite hemisphere. The *corpus callosum* (figure 1 and 2) is the most important of the commissural tracts and can be broken down into four parts: The rostrum (anterior most part) and the genu (anterior curvature) are made up of fibers connecting the anterior and ventral parts of the frontal lobes. The corpus (large middle portion) links posterior portions of the frontal lobes as well as the parietal lobes. The splenium (caudal curvature) enables communications between the temporal and occipital lobes.

Association tracts are bundles of axons connecting different regions of a given hemisphere. They are classified in two categories:

- Short association tracts (figure 1), the most common type of white matter in the cerebrum, connect adjacent gyri together. They are also called U-shaped fibers since they have to conform to the sulci shape separating adjacent gyri
- Long association tracts typically connect lobes within a hemisphere. One of the major association tracts is the superior longitudinal fasciculus, originating from the superior and middle temporal gyri and reaching the frontal lobe through the lateral fissure. This tract is of primary importance for speech and its alteration in the dominant hemisphere is known to induce a disconnection of the anterior speech area (Broca's area) and the posterior language area (Wernicke's area) with potential language disorders.

Projection tracts establish connections of the cerebral cortex with subcortical areas. The projection fibers of the *corona radiata* (figure 1), for example, connect cortical regions to the spinal cord and form a thick bundle called the internal capsule. A lesion in this area can produce severe sensory-motor deficits. Two types of projection tracts can be distinguished:

- Descending tracts carry motor commands from the motor cortex down to the muscles and glands through the lower brain structures and the spinal cord. They reach structures like the thalamus, the red nucleus, the medulla and serve muscle of the torso, extremities, facial and neck region.
- Ascending tracts carry sensory information from different parts of the body to the cerebral cortex. All sensory information, except olfactory, end up in the primary sensory areas of the cortex by the means of the thalamo-cortical fibers. The thalamus receives the somesthetic, gustatory, visual and auditory stimuli through these ascending pathways.

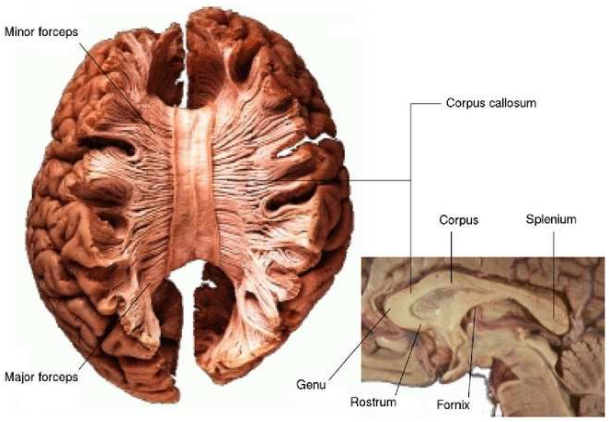

Figure 2: Dissection of the *corpus callosum* (from [64])

As we will step into the tractography problem, it will be fundamental to come back to the above mentioned properties of neural pathways (ie. connecting two precisely determined areas of the brain) and to model our algorithm to naturally take advantage of this fact.

2.2 Brownian Motion and Anisotropic Molecular Diffusion

As we will see in the following, diffusion MRI characterizes the anisotropic diffusion of water molecules in biological tissues which reflects their complex microstructure and, in particular, the geometry of neural pathways. We hereafter recall some properties of Brownian motion and molecular diffusion.

Brownian motion in Euclidean space is the simplest Markov process whose stochastic behavior is entirely determined by its initial distribution μ and its transition mechanism. Transitions are described by a probability density function p or an infinitesimal generator

$\mathcal{L}$. In linear homogeneous spaces, p is easily derived as the minimal fundamental solution associated with $\mathcal{L}$ (solution of equation 1). On manifolds, constructing this solution is a tough task, but for our problem, we only need to characterize $\mathcal{L}$. Further details can be found in [33]. We denote by $\mathbf{V}^d = \mathcal{C}([0,\infty[\rightarrow \mathbb{R}^d)$ the set of d-dimensional continuous functions

$$v : [0,\infty[\ni t \mapsto v(t) \in \mathbb{R}^d$$

and by $\mathcal{B}(\mathbf{V}^d)$ the topological σ-algebra on $\mathbf{V}^d$. Then, we have the

Definition 2.1 *A d-dimensional continuous process X is a $\mathbf{V}^d$-valued random variable on a probability space $(\Omega, \mathcal{F}, \mathbb{P})$*

By introducing the time $t \in [0,\infty[$, a time-indexed collection $\{X_t(\omega)\}$, $\forall \omega \in \Omega$ generates a d-dimensional continuous process if X_t is continuous with probability one. A Brownian motion is characterized by the

Definition 2.2 *With μ a probability on $(\mathbb{R}^d, \mathcal{B}(\mathbb{R}^d))$, $X_{t_0}, X_{t_1} - X_{t_0}, ..., X_{t_m} - X_{t_{m-1}}$ mutually independent with initial distribution specified by μ and Gaussian distribution for subsequent times (t_i are nonnegative and increasing), a process X_t is called a d-dimensional Brownian motion with initial distribution μ.*

X_t describing the position of water molecules, we now would like to understand how the diffusion behavior of these molecules is related to the underlying molecular hydrodynamics. Diffusion tensor, as thermal or electrical conductivity tensors, belongs to the broader class of general effective property tensors and is defined as the proportionality term between an averaged generalized intensity B and an averaged generalized flux F. In our particular case of interest B is the concentration gradient ∇C and F is the mass flux J such that Fick's law holds:

$$J = -\mathbf{D}\nabla C$$

By considering the conservation of mass, the general diffusion equation is readily obtained:

$$\frac{\partial C}{\partial t} = \nabla.(\mathbf{D}\nabla C) = \mathcal{L}C \tag{1}$$

In anisotropic cerebral tissues, water molecules motion varies in direction depending on obstacles such as axonal membranes. The positive definite order-2 tensor $\mathbf{D}$ has been related by Einstein [25] to the root mean square of the diffusion distance by

$$\mathbf{D} = \frac{1}{6t}\langle (x - x_0)(x - x_0)^T \rangle$$

($\langle . \rangle$ denotes an ensemble average). It actually turns out that the diffusion tensor measured by radioactive or fluorescent tracers is the same quantity that appears in the variance of the conditional probability distribution 2. This is directly related to the minimal fundamental solution of equation 1 for an unbounded anisotropic homogeneous medium with initial

distribution (obeying the same law as concentration) $\lim_{t\to 0} p(x|x_0,t) = \delta(x-x_0)$:

$$p(x|x_0,t) = \left(\frac{1}{4\pi|\mathbf{D}|t}\right)^{(d/2)} \exp\left(\frac{-(x-x_0)^T\mathbf{D}^{-1}(x-x_0)}{4t}\right) \quad (2)$$

Also known as the propagator, it describes the conditional probability to find a molecule, initially at position x_0, at x after a time interval t. All the above concepts find their counterparts when moving from linear spaces, such as $\mathbb{R}^d$, to Riemannian manifolds. Explicit derivation of p is non-trivial in that case and the Laplace-Beltrami operator will be of particular importance to define $\mathcal{L}$.
Diffusion MRI provides the unique method to non-invasively characterize molecular motion in biological tissues.

2.3 Diffusion Magnetic Resonance Imaging

2.3.1 The MRI Signal

Nuclear Magnetic Resonance (NMR) was simultaneously described by Bloch [12] at Stanford and Purcell [67] at Harvard in 1946. In 1971, it has been shown by Damadian, that relaxation times T1 and T2 of tumoral tissues are significantly longer than for the corresponding normal tissues. As soon as 1977, Mansfield [46] proposed a new ultrafast acquisition technique which will keep on improving: the echo-planar technique. Shortly after Bloch and Purcell discovery, Hahn published his seminal paper [30] on the NMR spin echo in which he noted that the random thermal motion of the spins would reduce the amplitude of the observed spin echo signal in the presence of a magnetic field inhomogeneity. Let us now recall the basics of MRI and its application to diffusion imaging.
All elementary particles rotating around a fixed axis (figure 3) possess a spin $\mathbf{s}$ aligned on its rotation axis whose effect is modelized by a magnetic dipole with moment $\mathbf{m}$. We then

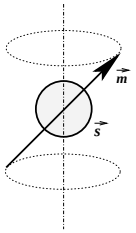

Figure 3: Nuclear spin aligned on its rotation axis and associated magnetic dipole

have the following relation: $\mathbf{m} = \gamma\mathbf{s}$ where γ is the gyromagnetic ratio which depends on the nucleus. Hydrogen has a gyromagnetic ratio of 42.58 MHz/T. Hydrogen has a high magnetic moment which gives rise to a resonance phenomenon. It is actually cumbersome to understand MRI on a microscopic scale. It is convenient, at a macroscopic level, to replace

the individual spin vectors by a single magnetization vector representing the spin of all the particles in a voxel (about 2.10^{15} protons/mm^3). The net resulting magnetization $\mathbf{M}$ is the sum of all the elementary moments and by making the assumption of a uniform distribution of the dipoles orientations in a given voxel, we simply end up with a $\mathbf{M} = 0$.
However, under the action of a static magnetic field $\mathbf{B_0}$ (from 1 and up to more than 9 Tesla, soon 11) along the z-axis, particles get aligned in the direction of that field and induce a magnetization parallel to $\mathbf{B_0}$ at equilibrium. In that state, the amplitude of $\mathbf{M}$ represents only a small fraction of what it would have been if all the particles were aligned in the same direction. Actually, by the laws of thermal dynamics the number of spins following the orientation imposed by $\mathbf{B_0}$ (low energy state) slightly outnumbers the amount of spins anti-parallel to the outer field (high energy state). The difference is small and given by:

$$\frac{N^-}{N^+} = e^{(-\frac{E}{kT})}$$

where N^- and N^+ are respectively the number of spins in the upper and lower states, k is the Boltzmann constant and T the temperature in Kelvin. Moreover, spins are not directly aligned with $\mathbf{B_0}$ but they have a precession motion around the direction of the magnetic field verifying

$$\frac{d\mathbf{m}}{dt} = \gamma \mathbf{m} \times \mathbf{B_0}$$

The precession frequency, known as the Larmor frequency is given by $\omega_o = \gamma|\mathbf{B_0}|$. For the nucleus we are interested in, hydrogen, the Larmor frequency in a field of $1.5T$ reaches 63.86 MHz. The net magnetization $\mathbf{M}$ can be decomposed into two components:

- $\mathbf{M_1}$ parallel to $\mathbf{B_0}$
- $\mathbf{M_2}$ orthogonal to $\mathbf{B_0}$ which becomes zero at equilibrium, for a given sample of molecules.

Resonance: By applying an oscillating electromagnetic (radio-frequency) pulse toward the area of the body to be examined, it is possible to compensate the difference in the number of atoms between the two energy states. The idea is to use a much weaker field than $\mathbf{B_0}$ at the Larmor frequency of the targeted nuclei and to apply it through a rotating reference frame orthogonal to $\mathbf{B_0}$. It causes the particles in that area to absorb the energy required to make them spin in a different direction and move from the lower energy state towards the higher. The exposure to the radio-frequency pulse causes the net magnetization to spiral away from $\mathbf{B_0}$. $\mathbf{M}$ rotates away from the longitudinal position in an amount proportional to the duration of the pulse. It is even possible to flip the original direction of $\mathbf{M}$. A pulse of 90 degrees would zero out the longitudinal component of $\mathbf{M}$. The net magnetization also starts to dephase since different particles experience a slightly different magnetic field. This is usually referred to as phase coherence. All the magnetic moments are in phase in their precession motion. The MRI signal is acquired by measuring a current induced in the plane where the radio-frequency pulse was applied. The frequency of this current is the Larmor

frequency of the nucleus and its amplitude is directly linked to the amount of magnetization in that plane.

Relaxation: By removing the radio-frequency pulse, particles begin to return to their initial energy state, aligned with the external field, from the higher to the lower. This is associated with a loss of stored excess energy to surrounding particles which can be detected by the coil of the MRI scanner. We can then observe two different types of relaxation processes:

- T1 weighted images follow the evolution of the increasing longitudinal component of **M**
- T2 weighted images follow the evolution of the decreasing transversal component of **M**

In clinical MRI, the radio-frequency pulse is typically chosen to coincide with the Larmor frequency of the hydrogen nucleus. The energy release during relaxation is thus an estimate of the number of protons or, in other words, the amount of water.

Spin-Lattice or **T1** relaxation is the consequence of an energy exchange between protons and the surrounding molecules. It is associated with the recovery of the initial longitudinal component of the net magnetization. The time constant **T1** comes from the fact that this process is modelized by an exponential law which, after a 90 degrees pulse, writes:

$$M_z = M_0(1 - e^{(\frac{t}{T1})})$$

63% of the longitudinal component is recovered after a time $T1$ and full recovery occurs after $5T1$.
Spin-Spin or **T2** relaxation reflects the energy exchange between surrounding protons and the loss of phase coherence. It is associated with the vanishment of the transversal component and is also modelized by an exponential law:

$$M_{xy} = M_0(e^{(\frac{t}{T2})})$$

63% of the transversal component has disappeared after a time $T2$. With these variables, it is possible to separate tissues since they will show different characteristics in $T1$ and $T2$ relaxation time.

2.3.2 Diffusion Magnetic Resonance Imaging

The standard pulse sequence that we just described is also called spin echo pulse sequence. After the preparation phase consisting of the 90 degrees radio-frequency pulse, the acquisition phase somehow boils down to a train of refocusing 180 degrees pulses which serve to generate repetitive (**T1**, **T2** or, as we are about to see, diffusion weighted) signal echoes (hence the name spin-echo). These pulses occur at times $\frac{1}{2}TE + iTE, \quad i = 1, ..., n$ and

signal acquisition is performed at times iTE (figure 4). The echoes serve to rephase all the coherences in the xy-magnetization which are lost during the time between 90 and 180 degrees pulses due to static magnetic field inhomogeneities intrinsic (i.e. susceptibility changes at tissue interfaces) and extrinsic (i.e. field inhomogeneities of the main magnetic field) to the examined object.

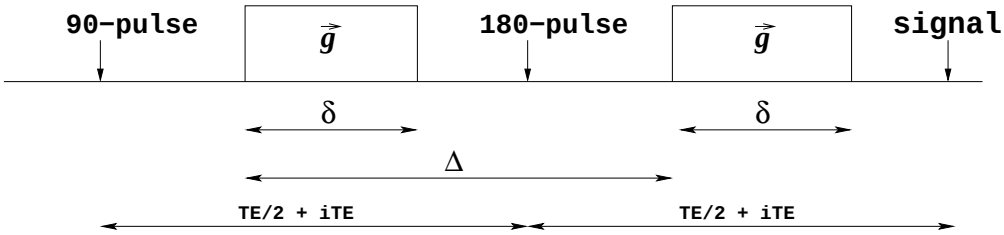

Figure 4: Stejskal-Tanner imaging sequence

To measure diffusion in several different directions, the Stejskal-Tanner imaging sequence [74] is used (figure 4). This sequence uses two gradient pulses, before and after a 180 degrees refocusing pulse controlling the diffusion weighting. The first gradient pulse causes a phase shift for all spins in the xy-plane; the second gradient pulse cancels this phase shift only for static spins. Spins under Brownian motion during the time period Δ undergo different phase shifts by the two gradient pulses resulting in a signal attenuation. For each slice, images are collected with different diffusion weightings and at least 6 independent gradient directions and 1 unweighted image. Each gradient is applied for several tenths of a millisecond during which the average water molecule may migrate 10 or more micrometers in a random direction. Diffusion can be estimated by using the equation [74]:

$$S = S_0 e^{(-bD)} \tag{3}$$

where b is the diffusion weighting factor proposed by Le Bihan et al. [40]:

$$b = \gamma^2 \delta^2 \left(\Delta - \frac{\delta}{3} \right) |\mathbf{g}|^2$$

with $|\mathbf{g}|^2$ the magnitude of the pulse, δ its duration and Δ the time separating two pulses.

2.4 Estimation and Regularization of DT MRI

As we will see during our numerical experimentations, the quality of the tensor field $\mathbf{T}$ computed from the diffusion weighted images is crucial for tractography. It mainly depends on an estimation phase, followed by a regularization step. Since those two problems are not the primary objective of this work, we just give a short overview of the methods involved.

Our dataset consists of 30 diffusion weighted images $S_k : \Omega \rightarrow \mathbb{R}$, $k = 1, ..., 30$ as

well as 1 image S_0 corresponding to the signal intensity in the absence of a diffusion-sensitizing field gradient (ie. $b = 0$ in equation 3). They were obtained on a GE 1.5 T Signa Echospeed with standard 22 mT/m gradient field. The echoplanar images were acquired on 56 evenly spaced axial planes with a 128×128 pixels in each slice. Voxel size is $1.875\ mm \times 1.875\ mm \times 2.8\ mm$. 6 gradient directions, each with 5 different magnitudes and 4 repetitions were used. Imaging parameters were: $b_{low} = 5\ s.m^{-2}$, $b_{high} = 1000\ s.m^{-2}$, TR $= 2.5\ s$, $TE = 84.4\ ms$ and a field of view of 24 cm [64]. Those data are courtesy of CEA-SHFJ/Orsay, France[1].

2.4.1 Estimation of Diffusion Tensors

We recall that the estimation of a field of 3×3 symmetric positive definite tensors $\mathbf{T}$ (ie. $\mathbf{T}(x) \in P(3)$) is done using the Stejskal-Tanner equation for anisotropic diffusion which is a direct generalization of equation 3 by simply replacing the scalar value D by the tensor $\mathbf{T}(\mathbf{x})$:

$$S_k(x) = S_0(x) e^{(-\gamma^2 \delta^2 (\Delta - (\delta/3)) \mathbf{g}_k^T \mathbf{T}(x) \mathbf{g}_k)} \quad \forall x \in \Omega \tag{4}$$

In order to estimate the six components of the tensors we need to choose six non-collinear gradients directions in addition to S_0 (where $\mathbf{g}_0 = (0,0,0)^T$). Our data have been acquired with the following classical orientations:

$$\mathbf{g}_1 = \tfrac{1}{\sqrt{2}}(1\ 1\ 0)^T \quad \mathbf{g}_2 = \tfrac{1}{\sqrt{2}}(1\ 0\ 1)^T \quad \mathbf{g}_3 = \tfrac{1}{\sqrt{2}}(0\ 1\ 1)^T$$
$$\mathbf{g}_4 = \tfrac{1}{\sqrt{2}}(1\ -1\ 0)^T \quad \mathbf{g}_5 = \tfrac{1}{\sqrt{2}}(1\ 0\ -1)^T \quad \mathbf{g}_6 = \tfrac{1}{\sqrt{2}}(0\ 1\ -1)^T$$

and the corresponding diffusion weighted images are presented on figure 5 below.
Many approaches have been proposed to estimate the tensor field. Westin et al. derived in [89] a compact analytical solution to equation 4. Simple multilinear regression by least squares fitting, robust methods [64] and variational estimation [81], [21], [80] (see figure 6) have also been used.

2.4.2 Regularization of Diffusion Tensor MRI

The variational framework for tensor estimation naturally brings some freedom to impose spatial coherency and smoothness into the generated tensor field. However, the fundamental properties of diffusion tensors, like diffusivities and principal orientations, are contained in their spectral features. Instead of directly smoothing the tensor field component-wise, it can be interesting to perform regularization with regard to those spectral elements. References can be found in [77], [78], [21], [79], [80], [2], [69], [13], [85] and [86].

[1]The authors would like to thank J.F. Mangin and J.B Poline for providing us with the data

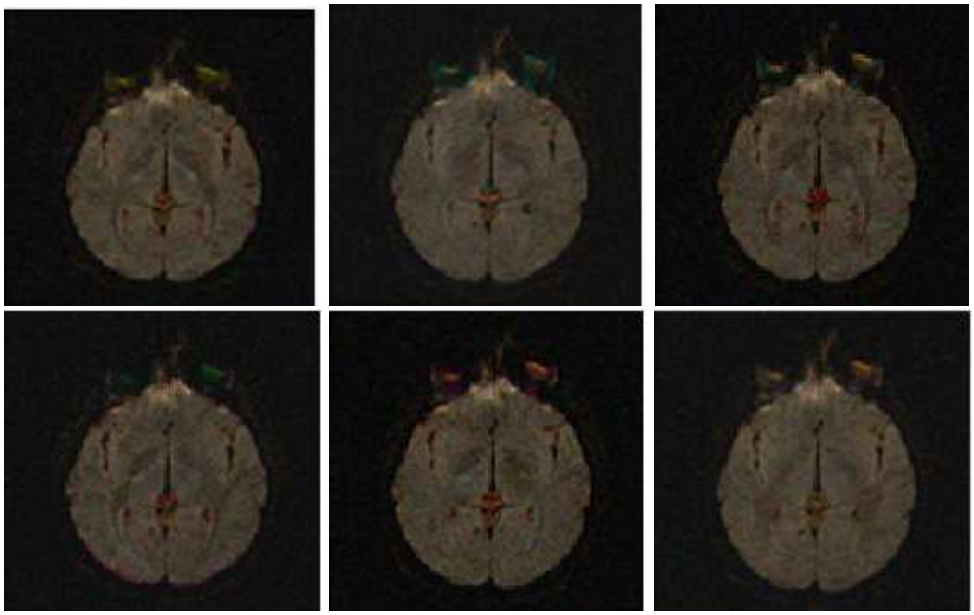

Figure 5: Diffusion Weighted images S_k $k = 1, ..., 6$

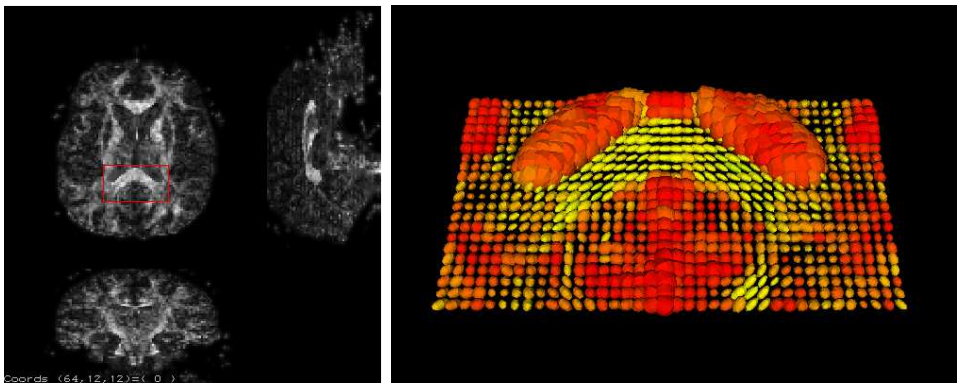

Figure 6: Results of the estimation by variational method

3 Connectivity Mapping

As we already exposed in the previous chapter, brain tissue is mainly composed of gray and white matter and, roughly speaking, the former contains processing centers while the latter is dedicated to the connection of the remote computational areas. Most normal brain functions require that specific cortical regions communicate with each other through fiber pathways. Until very recently, there was non non-invasive imaging method capable of resolving the white matter connections between those regions while functional MRI [75], [57], [4] or positron emission tomography [68] give us crucial information on the spatial localization of cerebral activation when a given task is performed. Moreover, even invasive methods based on chemical tracers do not typically enable reconstruction of line trajectories of fibers, making it difficult to assess the topographic connectivities within a pathway. Reliable estimation of these connections is thus fundamental if we want to better understand cerebral processes. Research has also started on the combined use of functional and diffusion MRI in order to show potential correlation between functional and anatomical connectivity [28].

The main idea on which relies classical tractography [52], [53], [64], [91] is that, despite the potentially multi-directional environment within a voxel, water diffusion in many regions of the white matter is highly anisotropic and consequently the orientation of the largest tensor eigenvector aligns with predominant axonal orientation [55], [63]. It should be safe to say that, accepting this restrictive assumption will enable us to identify macroscopical 3D architectures of the white matter. This gives rise to the line propagation technique that we have implemented and tested with various possible approaches. However, these local methods incorporate strong limitations and refinements have been proposed [10], [38], [39], [48], [82], [88], [14], [85]. More global algorithms [56], [61], [62], [17], stochastic modeling [11], [60], [29] or new acquisition methods were also introduced to try to overcome that restriction. We propose a novel global approach to tractography with strong theoretical justification by considering the white matter as a Riemannian manifold.

3.1 Line Propagation Techniques

3.1.1 Classical Streamline based Techniques

These techniques are the most intuitive since they simply propagate from a seed voxel by locally adapting the curve orientation to the vector field generated from the eigen decomposition of the diffusion tensor field. At each voxel, the eigenvector associated to the largest eigenvalue, reflects the microstructure of the underlying tissue and parallels the mean fiber orientation in that voxel. Then, as in fluid mechanics, the major eigenvector field is treated as a flow field and integrated in order to estimate streamlines, expected to coincide with white matter fibers. Denoting by $c(s)$ the trajectory parameterized by its arc-length, it can be simply computed as a 3D curve through linear integration, local tangent vector being given by the major eigenvector $\mathbf{u}^{[1]}$ of the diffusion tensor $\mathbf{D}$ at position $c(s)$. For a given

starting point c_0, we solve:

$$c(t) = c_0 + \int_0^t \mathbf{u}^{[1]}(c(s))ds \tag{5}$$

The integration is typically performed numerically with subvoxel precision through sufficiently small sizes Δs. In our implementation, we have used Euler and 2^{nd} or 4^{th} order Runge-Kutta schemes. For example, in the Euler case, we propagate by using the following scheme:

$$c_{r+1} = c_r + \mathbf{u}^{[1]}(c_r)\Delta s$$

forward and backward from the seeding point c_0. The higher-order methods seem to bring somehow more stability into the integration process but always, of course, within the strong limits of that approach and with a higher computational overhead.
The basic idea of the continuous approach (introduced by Mori et al. in [52] with the FACT algorithm) is to perform some interpolation of the vector field at each step inside a voxel in order to recover a smooth and more precise curve. However, we have to note that, because of the non unique eigen decomposition of the tensor, major eigenvectors are not always locally coherent (some may be flipped compared to their neighbors). There is thus a necessary and time consuming stage before every single interpolation, to make sure we actually combine coherent vectors.
In order to avoid that problem, we perform trilinear tensor interpolation and use the corresponding major eigenvector for integration. We have also integrated the anisotropy information in the interpolation process since we do not want an outlier tensor to corrupt that process. We have also incorporated some simple mechanism to refine the quality of the computed tract. For example, we can provide an anisotropy threshold under which we decide to stop the tracking process since that means that the local tangent vector is highly unreliable. We can also adjust the integration step Δs. We can also provide the tracking routine with an angle used to choose the direction of tracking in agreement with the previous steps. We may finally give an estimate of the length of the fibers to be computed so that very short fibers, undesirable for a clearer visualization, are automatically ignored.

To illustrate this, we have performed a tractography on figure 7 with a 4^{th} order Runge-Kutta scheme and trilinear interpolation weighted by linear anisotropy. The angle between consecutive integration steps was constrained to enforce a 70 degrees limit and fibers shorter than $1\,mm$ were not considered. The color applied to each fiber encodes the local degree of anisotropy (red is low, blue is high). The seeding voxels are those located inside the red box on the MRI image of figure 7. As we can see, despite the fairly tight starting region, the algorithm has propagated forward and backward and recovered the anterior *corpus callosum* as well as a few fibers from the right hemisphere *cingulum bundle* for a total of about 300 fibers.

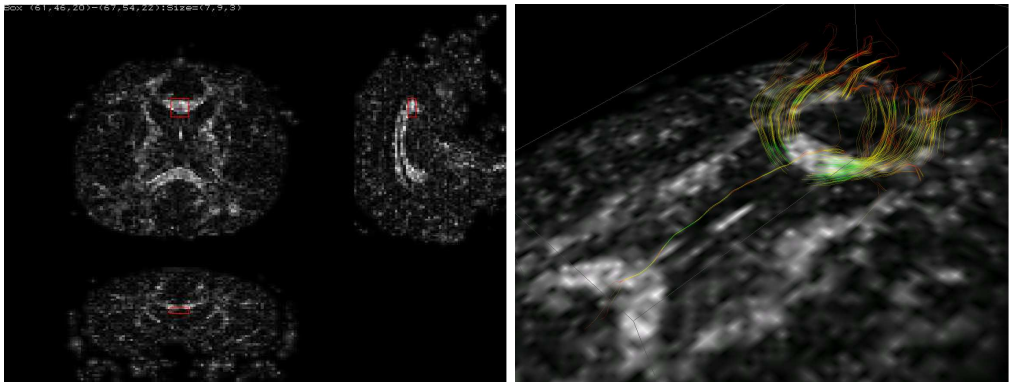

Figure 7: Brain Structures: Anterior part of the *corpus callosum* and right hemisphere *cingulum bundle*. Cutting plane: Axial slice of Linear Anisotropy

3.1.2 Advection-Diffusion based Techniques

Most current tractography studies use that streamline based approach, which seems to work well in many instances, even if the question of the validation is a tough issue here since ground truth data is limited. However, the method does suffer from a number of significant disadvantages. As Lazar et al. notice in [39], the noise that corrupts the diffusion MRI images will influence the directions of the major eigenvectors and thus lead an accumulation of errors during the integration. But most importantly, tractography may also be seriously affected by partial volume effects. Indeed, fibers of neighboring pathways very often cross each others. Thus considering the current resolution of diffusion MRI ($1mm$)and confronting it to the mean size of neural fibers (in the order of the micron), it seems obvious that in regions of fibers crossing, merging or fanning, the major eigenvector field cannot describe those complex structures.

We have thus implemented another method for tractography, based on the notion of tensor deflection. The idea is to consider the whole tensor to propagate through the diffusion tensor field in the most coherent fashion by incorporating information about the local orientation of the features. Our main problem, with partial volume effects, is that planar and spherical anisotropy yield a highly uncertain principal direction. In the extreme case, the tracking is stopped or the propagation becomes unstable. Using the whole tensor stabilizes the method by bringing some more information, comparable to a velocity term, hence the denomination advection-diffusion. We will denote by $\mathbf{v}_{in}$ and $\mathbf{v}_{out}$ respectively, the direction of propagation of the previous step and $\mathbf{v}_{out} = \mathbf{D}\mathbf{v}_{in}$. The direction of propagation to be estimated will be a weighted combination of those two vectors and the major eigenvector $\mathbf{u}^{[1]}$. By writing $\mathbf{v}_{in}$ in the local basis defined by the tensor at a given

voxel: $\mathbf{v}_{in} = \alpha_1\mathbf{u}^{[1]} + \alpha_2\mathbf{u}^{[2]} + \alpha_3\mathbf{u}^{[3]}$, we get

$$\mathbf{v}_{out} = \lambda_1 \left(\alpha_1\mathbf{u}^{[1]} + \frac{\lambda_2}{\lambda_1}\alpha_2\mathbf{u}^{[2]} + \frac{\lambda_3}{\lambda_1}\alpha_3\mathbf{u}^{[3]} \right)$$

So the tensor deflects the current propagation towards the major eigenvector while limiting curvature. We see that if the incoming vector coincides with one of the eigenvectors, the deflection has no effect on $\mathbf{v}_{out}$. For highly linear anisotropy, we see that $\mathbf{v}_{out} \approx \lambda_1\alpha_1\mathbf{u}^{[1]}$. If $\mathbf{D}$ is oblate shaped, the incoming eigenvector will be oriented towards that plane. If $\mathbf{D}$ is spherical, no deviation occurs. Then, using the normalized vectors $\mathbf{u}^{[1]}$, $\mathbf{v}_{in}$ and $\mathbf{v}_{out}$, the expression of the new direction of propagation is [88]:

$$\mathbf{v}_{prop} = c_l\mathbf{u}^{[1]} + (1 - c_l)((1 - w)\mathbf{v}_{in} + w\mathbf{v}_{out})$$

which handles all the cases cited above and provides some flexibility by the use of the weights c_l (linear anisotropy) and w (puncture). This last coefficient must be between 0 and 1 and says how much the algorithm, in the case of planar anisotropy, should turn into that plane. As proposed by Weinstein et al. [88] for diffusion imaging, a value of 0.2 seems to work well in practice. Another advantage of that approach is its speed, comparable to a regular Euler integration and much faster than a 4^{th} Runge-Kutta scheme. This enables us to produce the results on figure 8 where we chose seeding points in a small volume along the z-axis from the basis of the *corona radiata* up to the *corpus callosum*. About 8000 fibers where traced in less than 5 minutes and well-known brain structures like the *corpus callosum*, the *corona radiata* up to cortical regions, the internal capsule or the corticospinal tract could be easily identified. Of course, on synthetic data, it turns out that this algorithm performs better that the regular streamline based technique. On real MRI, it produces much smoother tracts when, for example, outlier tensors resulting from a incorrect estimation phase are present in a highly oriented tract.

3.1.3 Limitations and New Approaches

As we already stated, the assumption of voxel-wise homogeneous Gaussian diffusion on which relies the tensor model is restrictive and limits our capacity to resolve multiple fiber orientations per voxel. Streamline solutions are thus of very limited interest, advection-diffusion based schemes or other algorithms allowing to incorporate some constraints are more interesting. However, they do not provide any quantification of the strengths of connection and are, anyway, very sensitive to noise. Indeed, noise errors accumulate as the propagation keeps going and depends on the shape of the trajectory, anisotropy, resolution and interpolation method [37]. For example, in a helical trajectory model, the mean error after $10\,mm$ of tracking with regular, interpolation-based method is $0.002\,mm$ for infinite SNR and $0.40\,mm$ for a SNR of 30. By keeping in mind the difficulty of validation (for humans, most information has come from postmortem data on stroke patients), we now derive a new approach to white matter analysis, through the use of stochastic processes and differential geometry, which will yield physically motivated distance maps in the brain and thus the ability to compute intrinsic geodesics in the white matter.

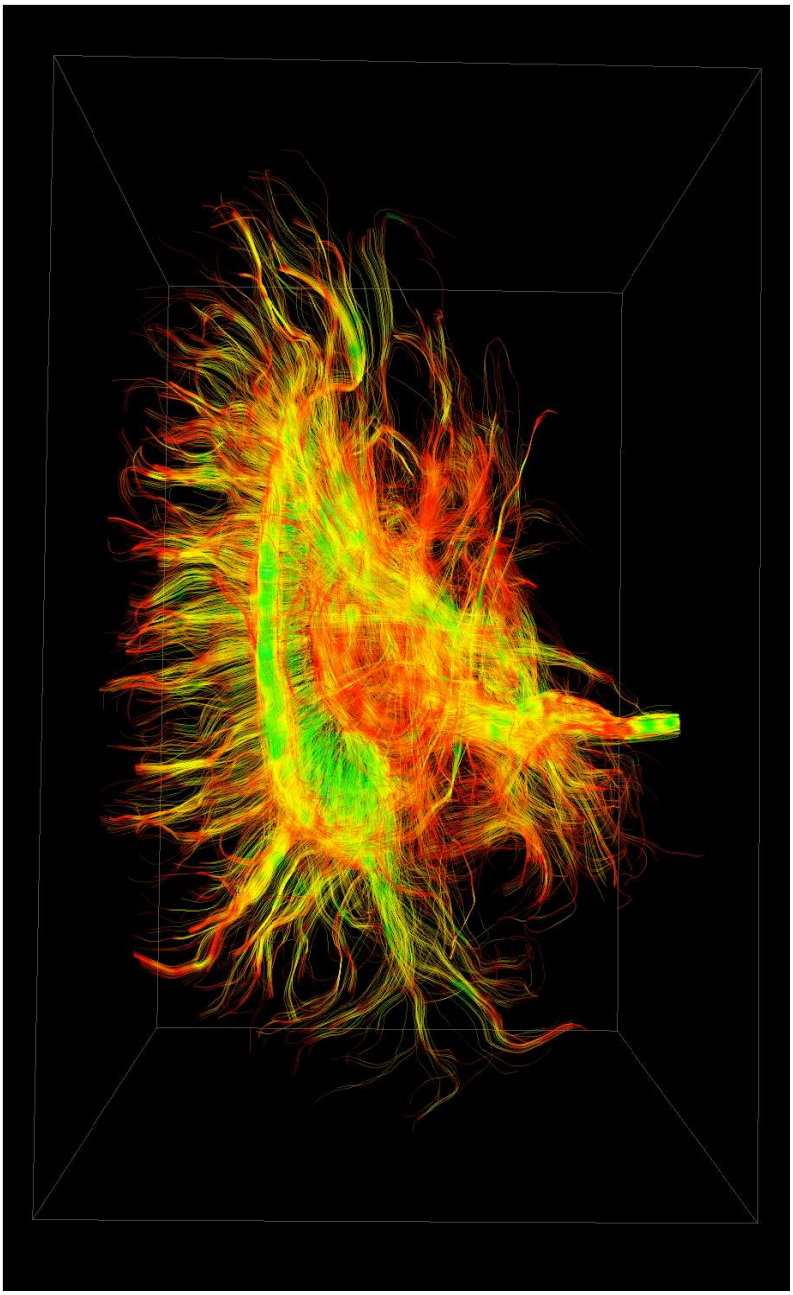

Figure 8: Tractography by our implementation of Advection-Diffusion based propagation (see [39])

3.2 White Matter as a Riemannian Manifold

We propose in this section a novel approach designed to consistently evaluate white matter connectivity in the brain from diffusion tensor data. Our goal here is to recast that challenging task into the natural framework of Riemannian differential geometry. A first attempt in that direction was made in [56]. Interesting results were proposed but no intrinsic characterization of the distance function on the manifold of interest was made. Other front propagation based methods for tractography were also proposed in [62] and [17].

3.2.1 Geometry of a Manifold from Diffusion Processes

We want to characterize the anisotropic diffusion of water molecules in the white matter exclusively in term of an appropriate infinitesimal generator $\mathcal{L}$ as described in section 2.2. Brownian motions are characterized by their Markovian property and the continuity of their trajectories. They have been described, in section 2, from their initial distribution μ and their transition density function p for homogeneous media, but they are more generally characterized in terms of $\mathcal{L}$-diffusion processes. We claim that under some technical hypothesis on $\mathcal{L}$ (with its domain of definition $D(\mathcal{L})$) and on the Brownian motion X_t, it is possible to define an $\mathcal{L}$-diffusion process on a Riemannian manifold M from the d-dimensional stochastic process X_t. We refer the interested reader to [22] and [33].

We focus, as in [22], on the case of a diffusion process with time-independent infinitesimal generator $\mathcal{L}$, assumed to be smooth and non-degenerate elliptic. We introduce Δ_M the Laplace-Beltrami differential operator such that, for a function f on a Riemannian manifold M:

$$\Delta_M f = \mathrm{div}(\mathrm{grad} f)$$

We will use the Einstein summation convention: When an index is repeated, once as a superscript and once as a subscript, a summation over this index is understood. In local coordinates $x_1, x_2, ..., x_d$, the Riemannian metric writes in the form

$$ds^2 = g_{ij} dx_i dx_j$$

and the Laplace-Beltrami operator becomes

$$\Delta_M f = \frac{1}{\sqrt{G}} \frac{\partial}{\partial x_j} \left(\sqrt{G} g^{ij} \frac{\partial f}{\partial x_i} \right) = g^{ij} \frac{\partial^2 f}{\partial x_i \partial x_j} + b^i \frac{\partial f}{\partial x_i}$$

where G is the determinant of the matrix $\{g_{ij}\}$ and $\{g^{ij}\}$ its inverse. Moreover,

$$b^i = \frac{1}{\sqrt{G}} \frac{\partial (\sqrt{G} g^{ij})}{\partial x_j} = g^{jk} \Gamma^i_{jk}$$

where Γ^i_{jk} are the Christoffel symbols of the metric $\{g_{ij}\}$. Δ_M is second order, strictly elliptic. At that point of our analysis, it turns out that constructing the infinitesimal generator $\mathcal{L}$ of our diffusion process boils down to (see [42]):

Definition 3.1 *The operator $\mathcal{L}$ is said to be an intrinsic Laplacian generating a Brownian motion on M if $\mathcal{L} = \frac{1}{2}\Delta_M$.*

Thus, for a smooth and non-degenerate elliptic differential operator on M of the form:

$$\mathcal{L} = \frac{1}{2} d_{ij} \frac{\partial^2}{\partial x_i \partial x_j}$$

we have the

Lemma 3.2 *If $\{d^{ij}\}_{i,j=1\ldots d}$ denotes the inverse matrix of $\mathbf{D} = \{d_{ij}\}_{i,j=1\ldots d}$, then $g = d^{ij} dx_i dx_j$ defines a Riemannian metric g on M.*

CONCLUSION: In the context of diffusion tensor imaging, this is of great importance for the following since it means that the diffusion tensor $\mathbf{D}$ estimated at each voxel actually defines, after inversion, the metric of the manifold. We have made the link between the diffusion tensor data and the white matter manifold geometry through the properties of Brownian motion. In the sequel, we will take $\mathbf{G} = \mathbf{D}^{-1}$.

3.2.2 From Radial Processes to Neural Fibers Recovery

We can now measure in the intrinsic space of the white matter. The fundamental idea of what follows consists of the hypothesis that water molecules starting at a given point x_0 on M, under Brownian motion, will potentially reach any point on M through a unique geodesic. The sole knowledge of the metric g will enable us to actually compute those geodesics on the manifold inferred from the Laplace-Beltrami operator. Considering paths of Brownian motion (ie. fibers in the white matter) as the characteristics lines of the differential operator $\mathcal{L}$ we can easily extend the concept of radial process for that type of stochastic motion on a Riemannian manifold M [32]. Let us fix a reference point $x_0 \in M$ and let $r(x) = \phi(x_0, x)$ be the Riemannian distance between x and x_0. Then we define the radial process $r_t = r(X_t)$. The function $r : M \to \mathbb{R}^+$ has a well behaved singularity at the origin. We make the assumption that M is geodesically complete and recall the notion of exponential map which will be of first importance for the numerical computation of neural fibers. We denote by c_e the geodesic with initial condition $c_e(0) = x$ and $c'_e(0) = e$ ($e \in T_x M$). We denote by $E \subset TM$ the set of vectors e such that $c_e(1)$ is defined. It is an open subset of the tangent bundle TM containing the null vectors $0_x \in T_x M$. We then state:

Definition 3.3 *The exponential map $\mathtt{exp} : E \subset TM \to M$ is defined by $\mathtt{exp}(e) = c_e(1)$. We denote by $\mathtt{exp}_x$ its restriction to one tangent space $T_x M$.*

Theorem 3.4 *(Hopf-Rinow) Let (M, g) be a Riemannian manifold.*

1. *Let $x \in M$. If the map $\mathtt{exp}_x$ is defined on the whole tangent space $T_x M$, then any point of M can be joined to x by a minimal geodesic.*
2. *If the manifold is geodesically complete, any two points of M can be joined by a minimal geodesic*

Hence, in particular, for each unit vector $e \in T_{x_0}M$, there is a unique geodesic $c_e : [0, \infty[\to M$ such that $c'_e(x_0) = e$ and the exponential map gives $c_e(t) = \mathtt{exp}_{x_0}(te)$. Then, if we identify $T_{x_0}M$, with $\mathbb{R}^d$, the exponential map becomes a map from $\mathbb{R}^d$ onto M. For small time steps t, the geodesics $c_e[0, t[$ is the unique distance minimizing geodesic between its endpoints. We need one more notion to conclude this section: the cutlocus of x_0, $\mathtt{Cut}_{x0}$, which will help us to characterize the distance function r. It is nothing but the locus of points where the geodesics starting orthonormally from x_0 stop being optimal for the distance. The radial function $r(x) = \phi(x_0, x)$ is Lipschitz on all M, smooth on $M/\mathtt{Cut}_{x0}$ where $|\mathrm{grad}\phi(x)| = 1$.

CONCLUSION: We have expressed the distance function on M. The objectives of the following section will be to propose accurate algorithms to compute this function ϕ everywhere on M and then to use it to estimate geodesics (Brownian paths) on this manifold (the brain white matter).

3.2.3 A Level Set Formulation for Intrinsic Distance Function

We are now concerned with the effective computation of the distance function ϕ from a closed, non-empty subset K of the 3-dimensional, smooth, connected and complete Riemannian manifold (M, g). In the remaining, K will actually be restricted to the single point x_0, origin of a Brownian motion. We will nevertheless formulate everything in term of K since considering the distance to a larger subset of M will be of interest for future work. Let us now further discuss the notion of distance function on a Riemannian manifold.

Given two points $x, y \in M$, we consider all the piecewise differentiable curves joining x to y. Since M is connected and complete, such curves do exist. To construct one of them, it is sufficient to cover a continuous curve joining x to y by a finite number of coordinates neighborhoods and replace each piece of curve contained in a coordinate neighborhood by a differentiable curve. We can then state the

Definition 3.5 *The distance $\phi(x, y)$ is defined as the infimum of the lengths of the C^1 curves starting at x and ending at y*

The topology induced by ϕ on M coincides with the original topology on M.

Corollary 3.6 *If $x_0 \in M$, the function $r : M \to \mathbb{R}$ given by $r(x) = \phi(x, x_0)$ is continuous on M but in general it is not everywhere differentiable.*

For instance, if M is compact, the distance function will be singular at the points of absolute maximum. For a complete analysis of the behavior of the distance function on the set where $D\phi$ does not exist, we refer the reader to [47] and [49].

We consider a general Hamilton-Jacobi partial differential equation with Dirichlet boundary conditions

$$\begin{cases} H(x, D\phi(x)) = 0 & \text{in } M \setminus K \\ \phi(x) = \phi_0(x) & \text{when } x \in K \end{cases}$$

where ϕ_0 is a continuous real function on K and the Hamiltonian $H : M \times T^\star M \rightarrow \mathbb{R}$ is a continuous real function on the cotangent bundle. We make the assumption that $H(x,.)$ is convex and we set $\phi_0(x) = 0 \; \forall x \in K$.

From the previous discussion, we are able to infer the metric g of the tangent bundle TM (which is dual to the metric on the cotangent bundle) from tensors characterizing the diffusion process on the manifold M and directly obtained through the estimation and regularization steps already presented. We denote by $|v|$ the magnitude of a vector v of TM, defined as $\sqrt{g(v,v)}$. In matrix notation, by forming $\mathbf{G} = \{g_{ij}\}$ the metric tensor, this writes $\sqrt{v^T \mathbf{G} v}$. Then, by setting $H(x,p) = |p| - 1$, we will work on the following theorem. For details on viscosity solutions on a Riemannian manifold, we refer to [47] and [49].

Theorem 3.7 *The distance function ϕ is the unique viscosity solution of the Hamilton-Jacobi problem*

$$\begin{cases} |grad\phi| = 1 & in\ M \setminus K \\ \phi(x) = 0 & when\ x \in K \end{cases} \tag{6}$$

in the class of bounded uniformly continuous functions.

This is the well-known eikonal equation on the Riemannian manifold (M, g). We quickly recall some important facts on viscosity solutions of PDE on manifolds (see [18] and [44] for more details). We begin with the definition of generalized differentials with Ω an open subset of M.

Definition 3.8 *Given a continuous function $u : \Omega \rightarrow \mathbb{R}$ and a point $x \in M$, the superdifferential of u at x is the subset of the cotangent space $T_x^\star M$ defined by*

$$\partial^+ u(x) = \{D\varphi(x) \; / \; \varphi \in C^1(M), \varphi(x) - u(x) = \min_M(\varphi - u)\}$$

Similarly the set

$$\partial^- u(x) = \{D\xi(x) \; / \; \xi \in C^1(M), \xi(x) - u(x) = \max_M(\xi - u)\}$$

is called the subdifferential of u at x. It is equivalent to replace the max *(*min*) on all M with the maximum (minimum) in an open neighborhood of x in M.*

Of course, if u is differentiable at $x \in M$, we have $\partial^+ u(x) = \partial^- u(x) = Du(x)$. We now give the definition of viscosity solution.

Definition 3.9 *We say that a continuous function u is a viscosity solution of equation*

$$H(x, Du(x)) = 0 \quad \forall x \in \Omega \subset M$$

if for every $x \in \Omega$

$$\begin{cases} H(x,v) \leq 0 & \forall v \in \partial^+ u(x) \\ H(x,v) \geq 0 & \forall v \in \partial^- u(x) \end{cases}$$

If only the first condition is satisfied (resp. the second), u is called a viscosity subsolution (resp. a viscosity supersolution).

The viscosity solution ϕ at $x \in M$ is the minimum time $t \geq 0$ for any curve γ to reach a point $\gamma(t) \in K$ starting at x with the conditions $\gamma(0) = 0$ and $|\frac{d\gamma}{dt}| \leq 1$. ϕ is the value function of the minimum arrival time problem. This will enable us to solve equation 6 as a dynamic problem and thus to take advantage of the great flexibility of Level Set methods. We must however say that the problem may be more naturally understood through its static formulation for which fast ordered upwind methods have been proposed and seem promising in terms of speed of convergence. This will be the object of a future work. References can be found in [65], [71] and [34].

On the basis of [58], [72], [76] and [15], we reformulate equation 6 in the Level Set perspective. The Level Set formulation easily treats self-intersections, topological changes and kinks. The main idea is to introduce a new function ψ in such a way that our evolving distance function ϕ_t is a level set of this function.

$$\phi_t = \{x \in M : \phi(x) = t\} = \{x \in M : \psi(x,t) = 0\}$$

It is actually a compact hypersurface of (M, g) dividing M into $\Gamma \subset M$ and its complement $\Gamma^c \subset M$. We call Γ the interior (the points of the manifold that have already been visited) and Γ^c the exterior (the points still unreached). In other words, one seeks a function $\psi(x,t)$ so that at $t = 0$, we have

$$\begin{cases} \psi(x,0) = 0 & \Leftrightarrow x \in \phi_0 \\ \psi(x,0) > 0 & \forall x \in \Gamma \\ \psi(x,0) < 0 & \forall x \in \Gamma^c \end{cases}$$

$\psi(x,0)$ is a uniformly continuous and monotonic strictly decreasing function of distance to ϕ_0 near ϕ_0. We then require that ϕ_t evolves so that

$$\psi(x,t) = 0 \Leftrightarrow t = \phi(x) \tag{7}$$

This allows us to generate $\phi(x)\ \forall x \in M$ by building it up through this level set formulation. Osher ([58]) showed by using Theorem 5.2 from [15] that, under the hypothesis that the Hamiltonian H is independent of ϕ, the level set generated by 7 is a viscosity solution to 6 if ψ is the viscosity solution of

$$\begin{cases} \psi_t + F(t,x,D\psi(t,x)) = 0 \quad \forall t > 0 \\ \psi(x,0) = \psi_0(x) \end{cases} \tag{8}$$

provided that $F > 0$ and does not change sign. This is typically the case for our anisotropic eikonal equation where the anisotropy directly arises from the manifold topology. To find our solution, all we need to do is thus to evolve $\psi(x,t)$ while tracking, for all x, the time $\bar{t}$ when it changes sign. Now we have to solve 8 with

$$F(t,x,D\psi) = H(t,x,D\psi) + 1 = |\mathrm{grad}\psi|$$

We first recall that for any function $f \in \mathbb{F}$, where $\mathbb{F}$ denotes the ring of smooth functions on M, the metric tensor $\mathbf{G}$ and its inverse define isomorphisms between vectors (in TM) and

1-forms (in $T^\star M$). In particular, the gradient operator is defined as

$$\text{grad}f = \mathbf{G}^{-1}df$$

where df denotes the first-order differential of f. It directly follows that

$$|\text{grad}\psi| = \sqrt{g(\text{grad}\psi, \text{grad}\psi)} = \left(g_{ij}\frac{\partial\psi}{\partial x_l}g^{li}\frac{\partial\psi}{\partial x_k}g^{kj}\right)^{1/2} = \left(\frac{\partial\psi}{\partial x_k}\frac{\partial\psi}{\partial x_l}g^{kl}\right)^{1/2}$$

and we now present the numerical scheme used to estimate the viscosity solution of

$$\psi_t + |\text{grad}\psi| = 0 \tag{9}$$

3.2.4 Numerical Scheme for the Distance Function

Numerical approximation of the hyperbolic term in 9 is now carefully reviewed. This Hamilton-Jacobi equation is similar to classical hyperbolic conservative laws and we will use this result to derive an accurate numerical scheme. We seek a three-dimensional numerical flux approximating the continuous flux $|\text{grad}\psi|^2$ and that is consistent and monotonous so that it satisfies the usual jump and entropy conditions and converges towards the unique viscosity solution of interest. For further details on this subject, the reader is referred to [41]. The good thing is that, for the 1-dimensional case, an Hamilton-Jacobi equation is strictly equivalent to a conservative law. This equivalence is usually lost when moving to higher dimensions. However, Barles [5] has shown that the solution obtained for an Hamilton-Jacobi equation stays the unique viscosity solution of the hyperbolic conservative equation associated to the jump and entropy conditions. We consider the hyperbolic conservative law

$$\frac{\partial u}{\partial t} + \frac{\partial f(u)}{\partial x} = 0 \tag{10}$$

The 1-dimensional Hamilton-Jacobi equation associated to the conservative law 10 is

$$\frac{\partial\phi}{\partial t} + f\left(\frac{\partial\phi}{\partial x}\right) = 0$$

and its approximation relies on the numerical flux $g(u_i^n, u_{i+1}^n) \approx f(u)$ with $u = \partial\phi/\partial x$. u_i^n,u_{i+1}^n are evaluated using appropriate finite differences schemes. We have used the Engquist-Osher numerical flux associated to a positive speed function and expressed for $f(u) = u^2$ as

$$g(u_1, u_2) = (\max^2(u_1, 0) + \min^2(u_2, 0))$$

We propose to extend this numerical flux to the 3-dimensional case for our quadratic Hamiltonian $D\psi^T\mathbf{G}^{-1}D\psi$ as follows

$$
\begin{aligned}
|\mathrm{grad}\psi|^2 = {} & g^{11}\left(\max^2(D^{x-}_{ijk}\psi,0)+\min^2(D^{x+}_{ijk}\psi,0)\right) \quad + \\
& g^{22}\left(\max^2(D^{y-}_{ijk}\psi,0)+\min^2(D^{y+}_{ijk}\psi,0)\right) \quad + \\
& g^{33}\left(\max^2(D^{z-}_{ijk}\psi,0)+\min^2(D^{z+}_{ijk}\psi,0)\right) \quad + \\
& 2g^{12}\left(\max(D^{x-}_{ijk}\psi,0)+\min(D^{x+}_{ijk}\psi,0)\right)\left(\max(D^{y-}_{ijk}\psi,0)+\min(D^{y+}_{ijk}\psi,0)\right) \quad + \\
& 2g^{13}\left(\max(D^{x-}_{ijk}\psi,0)+\min(D^{x+}_{ijk}\psi,0)\right)\left(\max(D^{z-}_{ijk}\psi,0)+\min(D^{z+}_{ijk}\psi,0)\right) \quad + \\
& 2g^{23}\left(\max(D^{y-}_{ijk}\psi,0)+\min(D^{y+}_{ijk}\psi,0)\right)\left(\max(D^{z-}_{ijk}\psi,0)+\min(D^{z+}_{ijk}\psi,0)\right)
\end{aligned}
$$

where $D^{x\pm}_{ijk}\psi = \frac{\pm(\psi_{(i\pm1)jk}-\psi_{ijk})}{\Delta x}$ is the upwind approximation of the gradient in x for instance.

This scheme is easily seen to be consistent. Cross-products of derivatives bring however some difficulties into the monotonicity analysis. As we will see in the following, the scheme does behave as expected even if it seems to be a little diffusive. We are currently working on the proof of monotonicity on the basis of the positiveness of $\mathbf{G}$.
Moreover, we have also experimented with higher order approximation schemes in order to increase the accuracy of the method. This is done by introducing WENO schemes in our numerical flux instead of the upwind gradients. WENO schemes are based on ENO (essentially non-oscillatory) schemes, which were first introduced by Harten, Osher, Engquist and Chakravarthy in [31] in the form of cell averages. They basically use a polynomial approximation of the derivatives and avoid oscillations when a shock is detected. WENO schemes of Liu, Osher and Chan [45], instead of approximating the numerical flux using the *best* candidate stencil, use a weighted convex combination of all the candidates stencils. We now quickly describe a very well-known method that speeds up the estimation of the distance function ϕ.

Narrow Band Method: In order to overcome the high computational overhead of the front propagation approach ($\mathcal{O}(N^3)$ if N denotes the number of grid points along a side), the narrow band method relies on the fact that it is sufficient to compute the level set function only in a small neighborhood (at a distance δ) around its zero level set because only this zero level set is physically meaningful (representing the interface). It was introduced by Chopp in [16]. In that case, the complexity drops to $\mathcal{O}(kN^2)$ in three dimensions, where k is the number of voxels in the band. In practice, at an iteration n, only the points in the band are updated and other points are kept intact. When the front moves near to the edge of the band, the calculation is stopped and a new band is initialized with the zero level set interface boundary at the center.

3.2.5 Numerical Schemes for the Geodesics Estimation

Now that we have our distance function ϕ on the manifold M with respect to the origin point x_0, we derive a classical and an intrinsic methods for geodesics computation in order to estimate paths of diffusion on M eventually corresponding to neural fibers tract. Geodesics are indeed the integral curves of the intrinsic distance function and are obtained by back-propagating along this function gradient field from a given point x towards the origin x_0. Our problem of interest consists of starting from a given voxel of the white matter and to compute the optimal pathway in term of the distance ϕ until x_0 is reached.
The simplest way to infer a geodesical path from ϕ is to backtrace on the manifold itself by solving the ordinary differential equation

$$\frac{dc(s)}{ds} = -\text{grad}\phi = -\mathbf{G}^{-1}D\phi \tag{11}$$

where c is the sought geodesic parameterized by s. gradϕ involves the metric of the cotangent space as well as the differential of the distance function $D\phi$, evaluated with appropriate finite difference schemes. We have experimented with Euler, 2^{nd} and 4^{th} order Runge-Kutta integration methods with sensibly better results obtained by higher order Runge-Kutta schemes but noticeable computational overheads. When integrating within a voxel, trilinear interpolation of ϕ is performed by using the 8 available values in the neighborhood.
However, this approach does not take into account the topology of the manifold on which we integrate. At each time step, we can leave this manifold and propagate this error as the integration process goes on. To make sure, we stay as close as possible to the domain on which we are computing the geodesics, we make use of the intrinsic exponential map `exp` of the Riemannian manifold which sends one-dimensional subspaces of the tangent space isometrically onto geodesics of M. Geometrically, $\texttt{exp}_x(e)$ is a point of M obtained by going out the length equal to $|e|$, starting from x, along the geodesic which passes through x with velocity equal to $e/|e|$. Then, if the geodesic $c(s)$ is the parameterized path $c(s) = (c_1(s), ..., c_d(s))$ which satisfies the differential equation

$$\frac{d^2c_i}{ds^2} = -\Gamma^i_{jk}\frac{dc_j}{ds}\frac{dc_k}{ds} \tag{12}$$

where Γ^i_{jk} are the Christoffel symbols of the second kind derived from the Riemannian metric g. They are used to study the geometry of the metric and also known as affine connection or connection coefficients. They are defined at each point $x \in M$ as

$$\Gamma^i_{jk} = \frac{1}{2}g^{il}\left(\frac{\partial g_{kl}}{\partial m_j} + \frac{\partial g_{jl}}{\partial m_k} - \frac{\partial g_{jk}}{\partial m_l}\right)$$

Equation 12 allows us to write `exp` in local coordinates around a point $x \in M$ as

$$\begin{aligned} \texttt{exp} : T_xM &\rightarrow M \\ c_i(\texttt{exp}(X)) &= X_i - \frac{1}{2}\Gamma^i_{jk}X_jX_k + \mathcal{O}(|X|^3) \end{aligned}$$

In our case $X \in T_x M$ will be identified with the gradient of the distance function at x and derivatives of the metric are estimated by appropriate finite difference schemes. This leads to a much more consistent integration scheme on M (though somehow more sensitive to noise because of the estimation of the derivatives of the metric).

3.2.6 Evaluation on Synthetic and Real Data

If local line propagation based methods only produce macroscopically satisfying results, our approach is more concerned to resolve local ambiguities due to isotropic tensors by incorporating global information through the distance function. We consider synthetic and real diffusion MRI data to validate the approach that we have just exposed. For each type of input, we will show the influence of the finite differences schemes on the quality of the computed distance function. Our criterion will be the *a posteriori* evaluated map $|\text{grad}\phi|$ which should equals 1 everywhere except around the origin x_0 where we know that the distance function is not differentiable. We will basically experiment with upwind and WENO5 schemes. Finally we will estimate the geodesics with the intrinsic method and conclude.

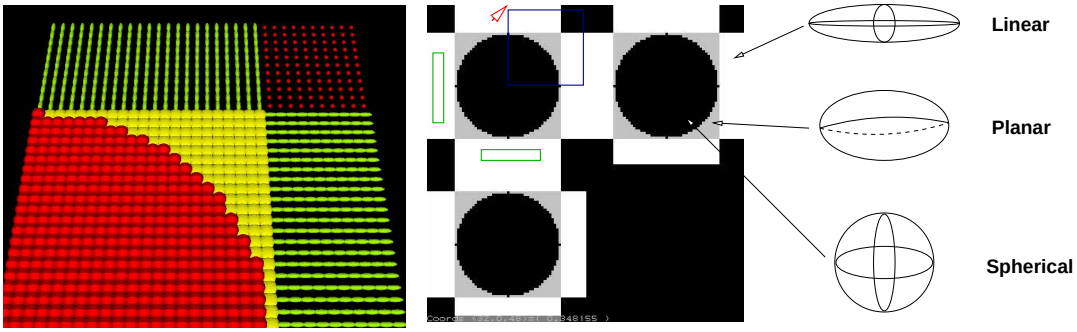

Figure 9: Synthetic tensors field. The rightmost column shows the three types of tensors. Central image represents (clockwise) an axial, sagittal and coronal slice of the linear anisotropy of the dataset. The leftmost picture shows the tensorial content of the blue box on the central image.

Synthetic Data: As shown on figure 9, synthetic data corresponds to an anisotropic non-homogeneous medium for which the diffusion paths describe three (independently homogeneous) intersecting three-dimensional cylinders. Actually, we have obtained those data by considering three $64 \times 64 \times 64$ volumes filled with isotropic (spherical tensors) and with anisotropic tensors inside a cylinder respectively along the x, y and z axis. These three volume were then summed voxel-wise. It results perfectly isotropic tensors at the intersection of the three cylinders, surrounded by planar tensors in the area where only two cylinders cross each others. Though very simple, this is a typical configuration where local methods

becomes totally unreliable. We choose the origin of the distance function x_0 at $(32, 32, 2)$ which we denote by the red arrow on figure 9. Geodesics will thus reach this voxel. We estimate the distance function ϕ with the level set scheme proposed in the previous section, first with upwind finite differences, then with WENO5 schemes. Figure 10 presents three slices (axial, sagittal and coronal and centered at $(32, 32, 32)$) of the distance function estimated with WENO5 schemes. The corresponding gradient field gradϕ is presented on figure

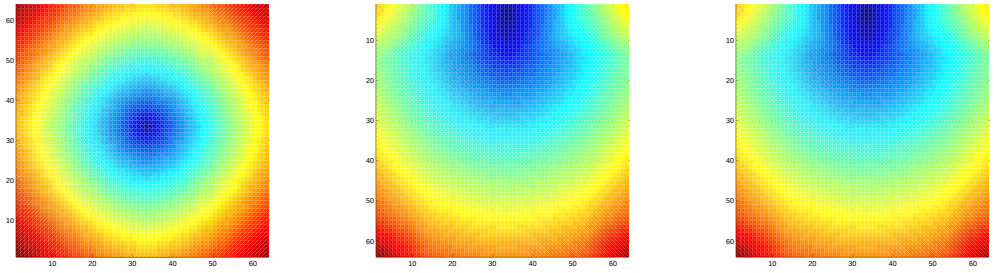

Figure 10: Estimated distance function for synthetic data

11 (clockwise axial, sagittal and coronal slices for each image and from left to right in the x, y and z directions). Results obtained with upwind differences are, of course, visually identical and not presented here. The estimations exhibit a good adequation with the expected results. Statistics in table 1 show results sensibly more accurate (smaller standard deviation and maximum reflecting a better behavior at the origin) for WENO5 schemes. The drawback is a higher computational overhead. Let us now try to recover the underlying

Scheme	**Mean**	**Std. Dev**	**Maximum**
Upwind	0.9854	0.123657	4.50625
WENO5	0.977078	0.116855	2.0871

Table 1: Statistics on |gradϕ| for synthetic data

pathways of the dataset towards x_0 (red arrow on figure 9). We have experimented with regular and intrinsic numerical integration techniques and they usually produce comparable results. The classical (Euler, Runge-Kutta) techniques require a small integration step to try to stick to the manifold and are thus computationally expensive. Our intrinsic method is much faster, though a bit more sensitive to noise. We are interested in seeing how the algorithm behaves while reaching the region where the cylinders cross. This is basically what happens in the brain white matter when multiple fiber bundles pass through a single voxel. We have initiated two tracking processes from the green and light blue areas indicated on figure 9. Results are presented on figure 12. The algorithm is hence capable of connecting the voxels of a single cylinder while passing through the intersection (left on figure 12), but it is also able to find the optimal paths connecting points of two different cylinders (right on

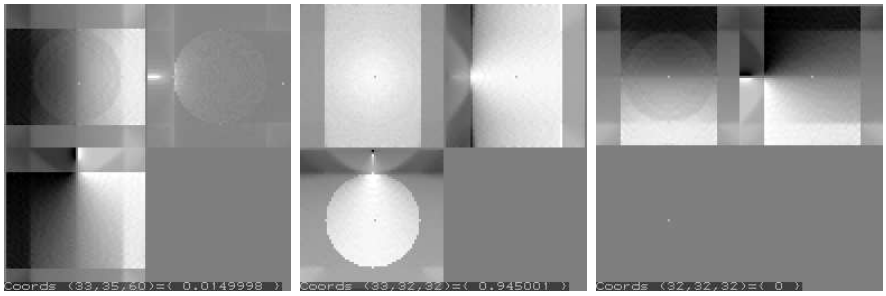

Figure 11: Synthetic data: Gradient gradϕ of the distance function on M used for geodesics inference

figure 12). Our global approach seems particularly adequate to disambiguate the problem of pathways crossings by minimizing the geodesic distance in the white matter.

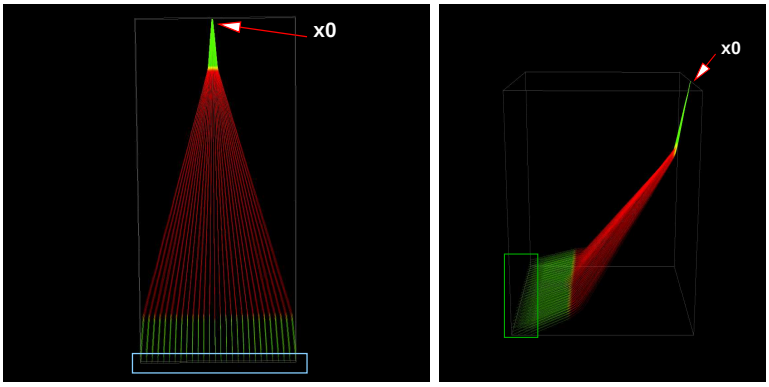

Figure 12: Synthetic data: Inferred geodesics by intrinsic integration

Diffusion MRI data: Real diffusion MRI data on figure 13 (left) is used to focus on the posterior part of the *corpus callosum* where highly organized white matter connects the two hemispheres together. Estimation of the distance function with upwind and WENO5 schemes produces again very good results with obvious advantage in term of robustness for WENO implementation (see statistics in table 2). Figure 13 (right) presents an axial slice passing through x_0 of the function ϕ estimated with the WENO scheme. The corresponding gradient field gradϕ is presented on figure 14. We must notice here that our numerical flux tends to be a bit diffusive, resulting in smooth distance functions. Fibers tracking from the voxels of the green box towards the red arrow of figure 13 (left) yields the results on figure 15 (left). Paths starting from low anisotropy regions are not computed. We have verified

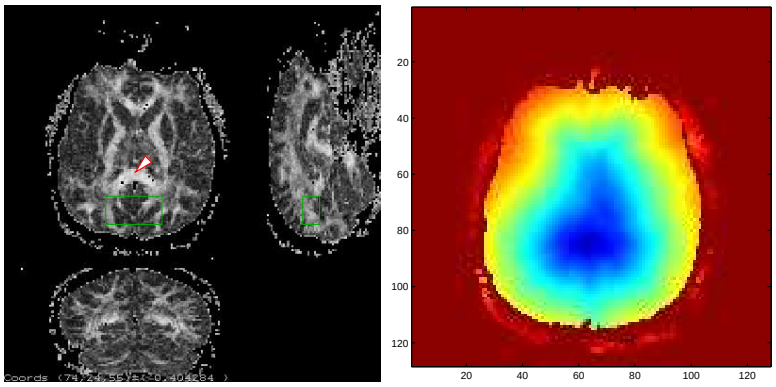

Figure 13: Diffusion tensor MRI data and axial slice of the estimated distance function

that the algorithm is not influenced at all by locally spherical or planar tensors. Indeed, the close up of figure 15 (right) indicates the presence of a low anisotropy region (red area) while the geometry of the fibers is not significantly affected by this configuration. Figure 16 shows another result of tractography performed in the area of the *corona radiata*. The distance function was computed with the origin x_0 in the *basis pedunculi* indicated by the red arrow. 10 voxels were selected in the cortical region indicated by the green box on figure 16 and the geodesics towards x_0 were estimated. The results present a good adequation with the dissection used as a reference. This global approach thus brings coherence into the diffusion tensor MRI data and naturally handles the issues affecting local tractography methods like inconsistent tracking in locally isotropic areas.

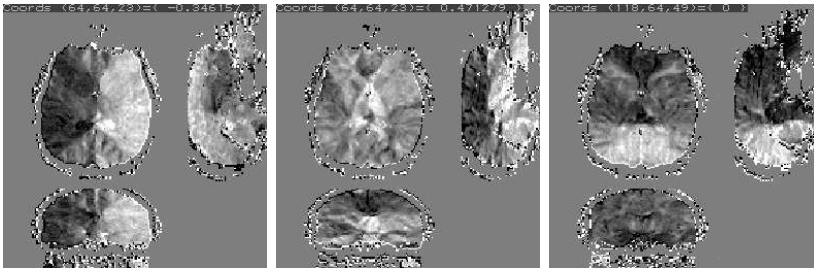

Figure 14: Diffusion MRI: Gradient gradϕ of the distance function on M

Scheme	Mean	Std. Dev	Maximum
Upwind	1.00568	0.249806	36.4311
WENO5	0.958425	0.198557	4.36123

Table 2: Statistics on |gradϕ| for real diffusion MRI data

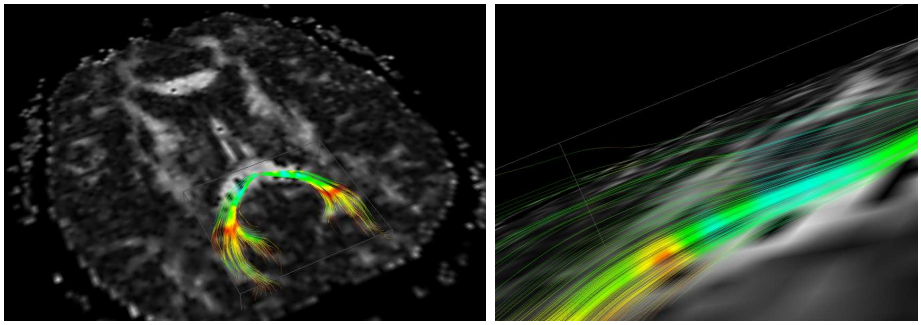

Figure 15: Diffusion MRI: Inferred geodesics by intrinsic integration

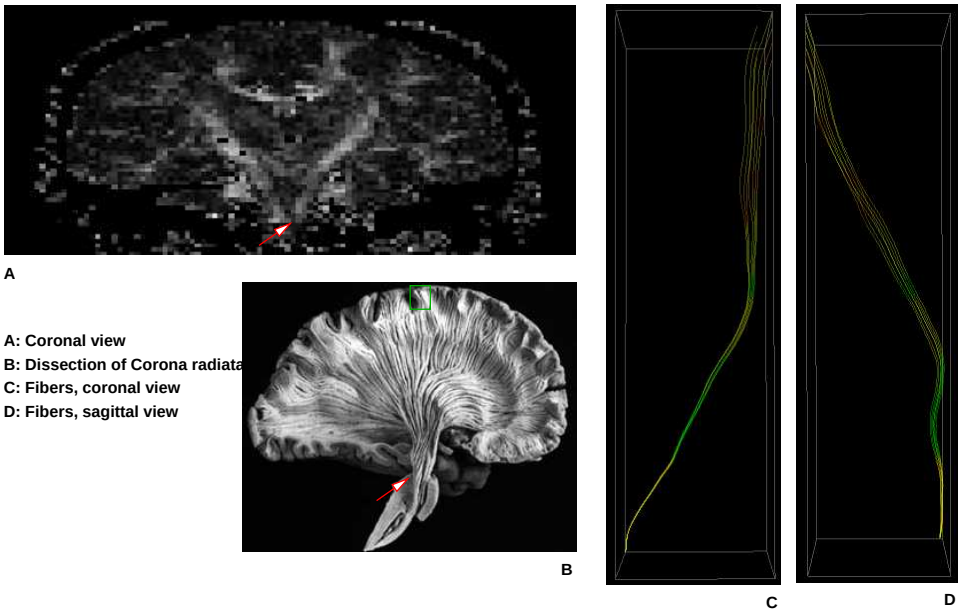

Figure 16: Diffusion MRI: Geodesics in the *corona radiata* (dissection image from [64])

4 Conclusion

Diffusion imaging is a quantitative method which gives a precise insight into the physical properties of tissues through the observation of random molecular motion. However correct interpretation of diffusion data and inference of accurate information is a very challenging project. The guideline of the novel approach to brain connectivity mapping developed in this report has been to always bear in mind that the true and unique phenomenon that diffusion imaging records is Brownian motion. Relying on the fact that probing and measuring a diffusion process on a manifold M provides enough information to infer the geometry of M (ie. the brain white matter), we can compute its geodesics, corresponding to diffusion pathways, hence fibers bundles. We have also implemented and evaluated some recent algorithms for tractography and compared them to our original approach which has shown good abilities for neural fibers tracking and for resolving fibers crossing problems inherent to diffusion tensor MRI. Clinical validation is obviously needed but already we can think of extensions of this method: intrinsic geodesics regularization under action of the scalar curvature of M or geodesics classification to recover complete tracts. Estimation of geodesics deviation could be used to detect merging or fanning fiber bundles. It will be ultimately interesting to fuse all this information with other modalities such as fMRI. Correlation between functional and anatomical connectivities is a typical application that would need to be investigated.

References

[1] G.W. Albers, M.G. Lansberg, A.M. Norbash, D.C. Tong, M.W. O'Brien, A.R. Woolfenden, M.P. Marks, M.E. Moseley, *Yield of diffusion-weighted MRI for detection of potentially relevant findings in stroke patients*, Neurology, 54:1562-1567, 2000

[2] L. Alvarez, P.L. Lions, and J.M. Morel, *Image selective smoothing and edge detection by nonlinear diffusion (II)*, SIAM Journal of Numerical Analysis, 29:845-866, 1992

[3] R. Bammer, M. Auer, S.L. Keeling, M. Augustin, L.A. Stables, R.W. Prokesch, R. Stollberger, M.E. Moseley, F. Fazekas, *Diffusion Tensor Imaging Using Single-Shot SENSE-EPI*, Magnetic Resonance in Medicine, 48:128-136, 2002

[4] P.A. Bandettini, E.C. Wong, R.S. Hinks, R.S. Tikofsky, J.S. Hyde, *Time Course EPI of Human Brain Function during Task Activiation*, Magnetic Resonance in Medicine, 25:390-397, 1992

[5] G. Barles, P.E. Souganidis *Convergence of Approximation Schemes for Fully Non-Linear Second Order Equations*, Asymptotic Analysis, 4:271-283, 1991

[6] P.J. Basser, J. Mattiello, D. LeBihan, *MR diffusion Tensor Spectroscopy and Imaging*, Biophysical Journal, 66:259-267, 1994

[7] P.J. Basser, J. Mattiello, D. LeBihan, *Estimation of the Effective Self-Diffusion Tensor from the NMR Spin Echo*, Journal of Magnetic Resonance, Series B, 103:247-254, 1994

[8] P.J. Basser, C. Pierpaoli, *Microstructural and Physiological Features of Tissues Elucidated by Quantitative-Diffusion-Tensor MRI*, Journal of Magnetic Resonance , 111:209-219, 1996

[9] P.J. Basser, *Relationships Between Diffusion Tensor and q-Space MRI*, Magnetic Resonance in Medicine, 47:392-397, 2002

[10] P.J. Basser, S. Pajevic, C. Pierpaoli, J. Duda, A. Aldroubi, *In Vivo Fiber Tractography Using DT-MRI Data*, Magnetic Resonance in Medicine, 44:625-632, 2000

[11] M. Bjornemo, A. Brun, R. Kikinis, C.F. Westin, *Regularized Stochastic White Matter Tractography Using Diffusion Tensor MRI*, Proccedings of Medical Imaging, Computing and Computer Assisted Intervention, LNCS 435-442, 2002

[12] F. Bloch, *Nuclear Induction*, Physical Review 70:460-474, 1946

[13] T. Brox, J. Weickert, *Nonlinear matrix diffusion for optic flow estimation*, DAGM-Symposium, 446-453, 2002

[14] J.S.W. Campbell, K. Siddiqi, B.C. Vemuri, G.B. Pike, *A Geometric Flow for White Matter Fibre Tract Reconstruction*, IEEE International Symposium on Biomedical Imaging, 505-508, 2002

[15] Y.G. Chen, Y. Giga, S. Goto, *Uniqueness and Existence of Viscosity Solutions of Generalized mean Curvature Flow Equations*, Journal of Differential Geometry, 33:749-786, 1991

[16] D.L. Chopp, *Computing Minimal Surfaces via Level Set Curvature Flow*, Journal of Computational Physics 106:77-91, 1993

[17] O. Cicarelli, A.T. Toosy, G.J.M. Parker, C.A.M Wheeler-Kingshott, G.J. Barker, D.H. Miller, A.J. Thompson, *Diffusion Tractography Based Group Mapping of Major White Matter Pathways in the Human Brain*, NeuroImage, 19:1545-1555, 2003

[18] M.G. Crandall, H. Ishii, P.L. Lions, *User's Guide to Viscosity Solutions of Second Order Partial Differential Equations*, Bulletin of American Mathematical Society, 27(1):1-67, 1992

[19] M.G. Crandall, P.L. Lions, *Viscosity Solutions of Hamilton-Jacobi Equations*, Transactions of American Mathematical Society, 277:1-43, 1983

[20] M. Cranston, W. Kendall, P. March, *The Radial Part of Brownian Motion II: Its Life and Times on the Cut Locus*, Probability Theory and Related Fields, 96:353-368, 1993

[21] C. Chefd'hotel, D. Tschumperlé, R. Deriche and O. Faugeras, *Constrained Flows of Matrix-Valued Functions : Application to Diffusion Tensor Regularization*, Proceedings of the European Conference on Computer Vision, 2002

[22] M.C. de Lara, *Geometric and Symmetry Properties of a Nondegenerate Diffusion Process*, Annals of Probability, 23(4):1557-1604, 1995

[23] Dejerine, *Anatomie des Centres Nerveux*, 1895

[24] M.P. Do Carmo, *Riemannian Geometry*, Birkhauser, Mathematics: Theory & Applications, 1992

[25] A. Einstein, *Investigations on the Theory of the Brownian Movement*, Dover 1926

[26] L.R. Frank, *Characterization of Anisotropy in High Angular Resolution Diffusion-Weighted MRI*, Magnetic Resonance in Medicine, 47:1083-1099, 2002

[27] S. Gallot, D. Hulin, J. Lafontaine, *Riemannian Geometry*, Springer-Verlag, 1990

[28] M. Guye, G. J.M. Parker, M. Symms, P. Boulby, C. A.M. Wheeler-Kingshott, A. Salek-Haddadi, G.J. Barker,J.S. Duncana, *Combined functional MRI and Tractography to Demonstrate the Connectivity of the Human Primary Motor Cortex in vivo*, NeuroImage, 19:1349-1360, 2003

[29] P. Hagmann, J.P. Thiran, L. Jonasson, P. Vandergheynst, S. Clarke, P. Maeder, R. Meuli, *DTI Mapping of Human Brain Connectivity: Statistical Fiber Tracking and Virtual Dissection*, NeuroImage, 19:545-554, 2003

[30] E.L. Hahn, *Spin echoes*, Physical Review, 80:580-594, 1950

[31] A. Harten, B. Engquist, S. Osher, S. Chakravarthy, *Uniformly High-order Accurate Essentially Non Oscillatory Schemes III*, Journal of Computational Physics, 71:231-303, 1987

[32] E.P. Hsu, *Stochastic Analysis on Manifolds*, Transactions of American Mathematical Society, 2002

[33] N. Ikeda, S. Watanabe, *Stochastic Differential Equations and Diffusion Processes*, North-Holland Mathematical Library, 1989

[34] C.Y. Kao, Stanley Osher, Y. Tsai, *Fast Sweeping Methods for a Class of static Hamilton-Jacobi Equations*, UCLA CAM Report 02-66, 2003

[35] J. Karger, W. Heink, *The Propagator Representation of Molecular Transport in Microporous Crystallites*, Journal of Magnetic Resonance Imaging, 51:1-7, 1983

[36] S. Kim, T.S. Kim, M. Singh, *MR Diffusion Tensor Imaging with Application to Conductivity Estimation*, preprint

[37] M. Lazar, A.L. Alexander, *Error analysis of white matter tracking algorithms for DT-MRI*, Proceedings of International Society of Magnetic Resonance in Medicine, 506, 2001

[38] M. Lazar, D. Weinstein, K. Hasan, A.L. Alexander, *Axon tractography with tensorlines*, Proceedings of International Society of Magnetic Resonance in Medicine, 482, 2000

[39] M. Lazar, D.M. Weinstein, J.S. Tsuruda, K.M. Hasan, K. Arfanakis, M.E. Meyerand, B. Badie, H.A. Rowley, V.Haughton, A. Field, A.L. Alexander, *White Matter Tractography Using Diffusion Tensor Deflection*, Human Brain Mapping, 18:306-321, 2003

[40] D. Le Bihan, E. Breton, D. Lallemand, P. Grenier, E. Cabanis, M. Laval-Jeantet, *MR Imaging of Intravoxel Incoherent Motions: Application to Diffusion and Perfusion in Neurologic Disorders*, Radiology, 161:401-407, 1986

[41] R.J. Leveque, *Numerical Methods for Conservative Laws*, Birkhauser, Basel, 1992

[42] M. Liao, *Symmetry groups of Markov processes*, Annals of Probabilities, 20:563-578, 1992

[43] C.P. Lin, V.J. Weeden, J.H. Chen, C. Yao, W.Y. I. Tseng, *Validation of Diffusion Spectrum Magnetic Resonance Imaging with Manganese-enhanced Rat Optic Tracts and ex Vivo Phantoms*, NeuroImage, 19:482-495, 2003

[44] P.L. Lions, *Generalized Solutions of Hamilton-Jacobi Equations*, Pitman, Boston, 1982

[45] X.D. Liu, S. Osher, T. Chan, *Weighted Essentially Non Oscillatory Schemes*, Journal of Computational Physics 115:200-212, 1994

[46] P. Mansfield, *Multi-planar Image Formation using NMR Spin Echoes*, Journal of Physics C, 10:55-58,1977

[47] C. Mantegazza, A.C. Mennucci, *Hamilton-Jacobi Equations and Distance Functions on Riemannian Manifolds*, Applied Mathematics and Optimization, 47(1):1-25, 2002

[48] T.E. McGraw, B.C. Vemuri, Y. Chen, M. Rao, T. Mareci, *Neuronal Fiber Tracking in DT-MRI*, preprint, 2002

[49] A.C. Mennucci, *Regularity and Variationality of Solutions to Hamilton-Jacobi Equations. part I: regularity*, preprint, 2002

[50] K.D. Merboldt, W. Hanicke, J. Frahm, *Self-diffusion NMR Imaging Using Stimulated Echoes*, Journal of Magnetic Resonance, 64:479-486, 1985

[51] M.M. Mesulam, *Tracing neural connections with horseradish peroxidase*, Wiley, 1982

[52] S. Mori, B.J. Crain, P.C. van Zijl, *3D Brain fiber reconstruction from diffusion MRI*, Proceedings of the International Conference on Functional Mapping of the Human Brain, 1998

[53] S. Mori, B.J. Crain, V.P. Chacko, P.C. van Zijl, *Three-dimensional Tracking of Axonal Projections in the Brain by Magnetic Resonance Imaging*, Annals of Neurology 45(2):265-269, 1999

[54] M.E. Moseley, Y. Cohen, J. Mintorovitch, J. Kucharczyk, J. Tsuruda, P. Weinstein, and D. Norman, *Evidence of Anisotropic Self-Diffusion*, Radiology, 176:439-445, 1990

[55] M.E. Moseley, Y. Cohen, J. Kucharczyk, J. Mintorovitch, H.S. Asgari, M.F. Wendland, J. Tsuruda, D. Norman, *Diffusion-weighted MR Imaging of anisotropic water diffusion in cat central nervous system*, Radiology, 176:439-445, 1999

[56] L. O'Donnell, S. Haker, C.F. Westin, *New Approaches to Estimation of White Matter Connectivity in Diffusion Tensor MRI: Elliptic PDEs and Geodesics in a Tensor-Warped Space*, Proccedings of Medical Imaging, Computing and Computer Assisted Intervention, LNCS 2488 459-466, 2002

[57] S. Ogawa, D.W. Tank, R. Menon, J.M. Ellerman, S.G. Kim, H.H. Merkle, K. Ugurbil, *Intrinsic Signal Changes Accompanying Sensory Stimulation: Function Brain Mapping with Magnetic Resonance Imaging*, Proceedings of the National Academy of Sciences, USA 89:5675-5679, 1992

[58] S. Osher, *A Level Set Formulation for the Solution of the Dirichlet Problem for a Hamilton-Jacobi Equations*, SIAM, Journal on Mathematical Anaysis., 24(5):1145-1152, 1993

[59] P.A. Osment, K.J. Packer, M.J. Taylor, J. J. Attard, T. A. Carpenter, L. D. Hall, S. J. Doran, N. J. Herrod, *NMR imaging of fluids in porous solids*, Philosophical Transactions of the Royal Society, 333:441-452, 1990

[60] G.J.M. Parker, D.C Alexander, *Probabilistic Monte Carlo Based Mapping of Cerebral Connections Utilising Whole-Brain Crossing Fibre Information*, Proceedings of Information Processing in Medical Imaging, 684-695, 2003

[61] G.J.M. Parker, *Tracing fibers tracts using fast marching*, Proceedings of the International Society of Magnetic Resonance, 85, 2000

[62] G.J.M. Parker, C.A.M. Wheeler-Kingshott, G.J. Barker, *Estimating Distributed Anatomical Connectivity Using Fast Marching Methods and Diffusion Tensor Imaging*, IEEE Transcations on Medical Imaging, 21(5):505-512, 2002

[63] C. Pierpaoli, P. Jezzard, P.J. Basser, A. Barnett, G. Di Chiro, *Diffusion Tensor MR Imaging of Human Brain*, Radiology, 201:637-648, 1996

[64] Cyril Poupon, *Détection des faisceaux de fibres de la substance blanche pour l'étude de la connectivité anatomique cérébrale*, Ecole Nationale Supérieure de Telecommunications de Paris, 1999

[65] E. Prados, O. Faugeras, *A Mathematical and Algorithmic Study of the Lambertian Shape from Shading Problem for Orthographic and Pinhole Cameras*, INRIA Research Report, 2003

[66] K. Pribam, P. MacLean, *Neuronographic analysis of medial and basal cerebral cortex*, Journal of Neurophysiology, 16:324-340, 1953

[67] E.M. Purcell, H.C. Torrey, R.V. Pound, *Resonance Absorption by Nuclear Magnetic Moments in a Solid*, Physical Review 69:37-38, 1946

[68] M.E. Raichle, *Images of the Mind: Studies with Modern Imaging Techniques*, Annual Review of Psychology, 45:333-356, 1994

[69] G. Sapiro, *Geometric Partial Differential Equations and Image Analysis*, Cambridge University Press, 2001

[70] N.R. Selden, D.R. Gitelman, N. Salamon-Murayama, T.B. Parrish, M.M. Mesulam, *Trajectories of Cholinergic Pathways within the Cerebral Hemispheres of the Human Brain*, Brain, 121:2249-2257, 1998

[71] J.A. Sethian, A. Vladimirsky, *Ordered Upwind Methods for Static Hamilton–Jacobi Equations: Theory and Algorithms*, SIAM Journal on Numerical Analysis, 41(1):325-363, 2003

[72] J.A. Sethian, *Level Set Methods and Fast Marching Methods: Evolving interfaces in computational geometry, fluid mechanics, computer vision and material science*, Cambridge University Press, 1996

[73] C. Sotak, *The Role of Diffusion Tensor Imaging (DTI) in the Evaluation of Ischemic Brain Injury*, Nuclear Magnetic Resonance in Biomedicine 15:561-569, 2002

[74] E.O. Stejskal, J.E. Tanner, *Spin Diffusion Measurements: Spin Echoes in the Presence of a Time-dependent Field Gradient*, Journal of Chemical Physics, 42:288-292, 1965

[75] B. Thirion, O. Faugeras, *Activation Detection and Characterisation in Brain fMRI Sequences: Application to the Study of Monkey Vision.*, INRIA Research Report, 2001

[76] Y.H. Tsai, Y. Giga, S. Osher, *A Level Set Approach for Computing Discontinuous Solutions of A Class of Hamilton-Jacobi Equations*, to appear in Mathematics of Computations, 2003

[77] D. Tschumperlé, R. Deriche, *Orthonormal Vector Sets Regularization with PDE's and Applications*, International Journal on Computer Vision, 2002

[78] D. Tschumperlé, R. Deriche, *DT-MRI Images: Estimation, Regularization and Application*, Proceedings of International Conference on Computer Aided Systems Theory, January 2003

[79] D. Tschumperlé, R. Deriche, *Diffusion Tensor Regularization with Constraints Preservation*, Proceedings of Computer Vision and Pattern Recognition, 2001

[80] D. Tschumperlé, R. Deriche, *Regularization of orthonormal vector sets using coupled PDE's*, IEEE Workshop on Variational and Level Sets Methods in Computer Vision, 2001

[81] D. Tschumperlé, R. Deriche, *Variational Frameworks for DT-MRI Estimation, Regularization and Visualization*, Proceedings of International Conference on Computer Vision, 2003

[82] D.S. Tuch, *Mapping cortical connectivity with diffusion MRI*, Proceedings of IEEE International Symposium on Biomedical Imaging, 392-394, 2002.

[83] D.S. Tuch, T.G. Reese, M.R. Wiegell, N.G. Makris, J.W. Belliveau, and V.J. Wedeen, *High angular resolution diffusion imaging reveals intravoxel white matter fiber heterogeneity*, Magnetic Resonance Medicine, 48:577-582, 2002.

[84] D.S Tuch, V.J Wedeen, A.M Dale, J.S George, J.W Belliveau, *Conductivity Tensor Mapping of the Human Brain using Diffusion Tensor MRI*, Proceedings of the National Academy of Sciences, USA, 98:11697-11701, 2001

[85] B. Vemuri, Y. Chen, M. Rao, T. McGraw, T. Maerci, Z. Wang, *Fiber Tract Mapping from Diffusion Tensor MRI*, IEEE Workshop on Variational and Level Sets Methods in Computer Vision, 2001

[86] Z. Wang, B. Vemuri, Y. Chen, T. Maerci, *Simultaneous Smoothing and Estimation of the Tensor Field from Diffusion Tensor MRI*, Proceedings of IEEE Conference on Computer Vision and Pattern Recognition, 461-466, 2003

[87] A.E. Baird, S.Warach, *Magnetic Resonance Imaging of Acute Stroke*, Journal of Cerebral Blood Flow Metabolism 18:582-609, 1998

[88] D.M. Weinstein, G.L. Kindlmann, E.C. Lundberg, *Tensorlines: Advection-Diffusion based Propagation Through Tensor Fields*, IEEE Visualization, 249-253, 1999

[89] C.F. Westin, S.E. Maier, H. Mamata, A. Nabavi, F.A. Jolesz, and R. Kikinis, *Processing and visualization for diffusion tensor MRI*, Proceedings of Medical Image Analysis, 6:93-108, 2002

[90] M. Young, J. Scannell, G. Burns, *The Analysis of Cortical Connectivity*, Neuroscience Intelligence Unit, Springer Verlag, 1995

[91] L. Zhukov, A.H. Barr, *Oriented Tensor Reconstruction: Tracing Neural Pathways from Diffusion Tensor MRI*, IEEE Visualization, 2002

Unité de recherche INRIA Sophia Antipolis
2004, route des Lucioles - BP 93 - 06902 Sophia Antipolis Cedex (France)

Unité de recherche INRIA Futurs : Parc Club Orsay Université - ZAC des Vignes
4, rue Jacques Monod - 91893 ORSAY Cedex (France)
Unité de recherche INRIA Lorraine : LORIA, Technopôle de Nancy-Brabois - Campus scientifique
615, rue du Jardin Botanique - BP 101 - 54602 Villers-lès-Nancy Cedex (France)
Unité de recherche INRIA Rennes : IRISA, Campus universitaire de Beaulieu - 35042 Rennes Cedex (France)
Unité de recherche INRIA Rhône-Alpes : 655, avenue de l'Europe - 38334 Montbonnot Saint-Ismier (France)
Unité de recherche INRIA Rocquencourt : Domaine de Voluceau - Rocquencourt - BP 105 - 78153 Le Chesnay Cedex (France)

Éditeur
INRIA - Domaine de Voluceau - Rocquencourt, BP 105 - 78153 Le Chesnay Cedex (France)
http://www.inria.fr
ISSN 0249-6399